MID-AMERICA
TRANSPORTATION CENTER

Report # MATC-MS&T: 133-2

Final Report
WBS: 25-1121-0005-133-2

Repair of Corroded Steel H-Piles Using High Performance Material - Phase II

Mohamed A. ElGawady, PhD
Professor

Mohanad M. Abulazeez
PhD candidate

Eslam Gomaa
PhD student

Amro Ramadan
PhD student

Mahmood Tousif
PhD candidate

Binod Sherstha
PhD student

Department of Civil, Architectural
& Environmental Engineering
Missouri University of Science and Technology

2021

A Cooperative Research Project sponsored by
U.S. Department of Transportation- Office of the Assistant
Secretary for Research and Technology

Repair of Corroded Steel H-Piles Using High Performance Material – Phase II (UHPC and FRP Repair Sections

Mohamed A. ElGawady, Ph.D.
Professor
Department of Civil, Architectural &
Environmental Engineering
Missouri University of Science and
Technology

Binod Sherstha
Ph.D. student
Department of Civil, Architectural &
Environmental Engineering
Missouri University of Science and
Technology

Mohanad M. Abulazeez
Ph.D. candidate
Department of Civil, Architectural &
Environmental Engineering
Missouri University of Science and
Technology

Eslam Gomaa
Ph.D. student
Department of Civil, Architectural &
Environmental Engineering
Missouri University of Science and
Technology

Amro Ramadan
Ph.D. student
Department of Civil, Architectural &
Environmental Engineering
Missouri University of Science and
Technology

Mahmood Tousif
Ph.D. candidate
Department of Civil, Architectural &
Environmental Engineering
Missouri University of Science and
Technology

A Report on Research Sponsored by

Mid-America Transportation Center

University of Nebraska-Lincoln

November 2021

TECHNICAL REPORT DOCUMENTATION PAGE.

1. Report No.: 25-1121-0005-133-2	2. Government Accession No.:	3. Recipient's Catalog No.:
4. Title and Subtitle: Repair of Corroded Steel H-Piles Using High Performance Material – Phase II (UHPC and FRP Repair Sections)		5. Report Date: Nov 2021 6. Performing Organization Code:
7. Author(s): Mohanad M. Abdulazeez, Amro Ramadan, Binod Sherstha, Eslam Gomaa, Mahmood Tousif, and Mohamed A. ElGawady, ORCID: 0000-0001-6928-9875		8. Performing Organization Report No.: 25-1121-0005-133-2
9. Performing Organization Name and Address: Mid-America Transportation Center 2200 Vine St. PO Box 830851 Lincoln, NE 68583-0851		10. Work Unit No.: 11. Contract or Grant No.: 69A3551747107
12. Sponsoring Agency Name and Address: Missouri University of Science and Technology 300 W 13th St Rolla, MO 65409		13. Type of Report and Period Covered: Final Report Jan 2019 – Sept 2020 14. Sponsoring Agency Code: MATC TRB RiP No. 91994-40
15. Supplementary Notes: The investigation was conducted in cooperation with the Missouri Department of Transportation, U.S. Department of Transportation, Federal Highway Administration.		

16. Abstract:

This report summarizes the details of experimental work conducted to evaluate the performance of repaired-after-corrosion H-piles. Six full-scale H-piles were investigated under concentric loads. The piles had milled cross-sections to represent the loss of a cross-sectional area due to corrosion. Two different repair solutions were investigated: concrete-filled pultruded fiber reinforced polymer tubes (CFPTs) and ultra-high performance concrete (UHPC) plates. A push-out test of fourteen specimens was carried out to optimize the two repair techniques. This was followed by repairing six full-scale H-piles using the two different methods. The UHPC plates repair approach was able to recover the strength of the corroded piles. The UHPC, however, represented a fast repair solution. Concrete filled pultruded FRP tubes repair was not able to recover the strength of the virgin piles. The concrete-filled pultruded FRP tubes solution was not able to recover the strength of the repaired pile.

17. Key Words: Steel H-piles, UHPC, Pultruded CFRP, Corrosion		18. Distribution Statement: No restrictions. This document is available to the public through National Technical Information Center, Springfield, Virginia 22161.	
19. Security Classification (of this report): Unclassified.	20. Security Classification (of this page): Unclassified.	21. No of Pages: 81	22. Price:

Table of Contents

List of Figures

List of Tables

Acknowledgments

The authors would like to acknowledge the many individuals and organizations that made this research project possible. The authors wish to extend a sincere thank you to the Mid-America Transportation Center (MATC) and Missouri Department of Transportation (MoDOT). In addition to their financial support, the authors appreciate MoDOT’s vision and commitment to innovative concepts and pushing the boundaries of current practice.

The authors would also like to thank Skyline Steel that provided material contributions necessary for the successful completion of this project. Finally, the authors would like to thank the many students at Missouri S&T for their valuable contributions to the research. The authors also appreciate the tireless staff of the Department of Civil, Architectural, and Environmental Engineering and the Center for Infrastructure Engineering Studies. Their assistance both inside and out of the various laboratories was invaluable to this project's successful completion.

Executive Summary

This report summarizes the details of experimental work conducted to evaluate the performance of six repaired-after-corrosion H-piles. Two different repair approaches were investigated. The first approach included attaching concrete-filled pultruded fiber reinforced polymer tubes to the corroded pile. The second option included attaching ultra-high performance concrete plates to the corroded piles. The two solutions were first optimized using push-out testing of fourteen steel H-piles. This was followed by repairing six full-scale piles and subjecting them to concentric axial loads. This comprehensive research revealed that specimens repaired using UHPC plates were able to recover their virgin strengths. In addition, the UHPC plate solution is a versatile solution that can be used for rapid repair. The concrete-filled pultruded FRP tubes solution was not able to recover the strength of the repaired pile.

Chapter 1 Introduction

H-piles are a common type of deep foundation in the bridge industry that can be embedded or protruded. The cross-sectional area of an H-pile is relatively small; consequently, it can be driven through compacted granular materials and soft rocks with limited effect on ground swelling or rising of adjacent piles (Hannigan et al. 2016). H-piles embedded in relatively impervious earth that is deeper than two feet below the ground surface are mostly free of corrosive effects because of the insufficient oxygen presence. Embedded H-piles, however, may be subjected to corrosion when the surrounding medium has low pH values, such as in alkaline soils. Furthermore, H-piles protruding from the ground are exposed to corrosion at the surface and below the ground line. H-piles exposed to water and salts can also suffer severe deterioration in the splash zone. Salts can migrate to the pile's surface either from the water or due to the use of deicing solutions (Romanoff 1962).

There are numerous bridges in the United States that have H-piles with various corrosion levels caused by environmental conditions (FHWA 2015). Therefore, these piles do not meet the current axial load demands and need to be repaired or replaced. While corrosion may extend over a limited length and section of a pile, it can also be quite extensive, causing severe loss of a pile’s cross-section over a significant length. The severity of the corrosion is key to determining the H-pile's residual capacity and determining whether the H-pile can be repaired or should be replaced. Therefore, the behavior of corroded piles under axial loads needs to be better understood.

1.1 Corrosion Classification and Assessment

Researchers have been developing different methods such as experimental, analytical, and non-linear analysis to classify the corrosion levels and predict the capacity of corroded elements with different steel sections under different loading protocols to achieve precision in determining the appropriate solution for the corroded section (Beaulieu et al. 2010; Bruneau et al. 1998; Bruneau and Zahrai 1997; Jiang and Soares 2012; Jiang and Soares 2012; Karagah et al. 2015; Kayser and Nowak 1989; Liu et al. 2005; Ok et al. 2007; Paik et al. 2003; Ramadan 2020; Ramadan and ElGawady 2019; Saad-Eldeen et al. 2011).

1.2 Repair Methods Used in the Current Report

Based on corrosion intensity, performance objectives, and feasibility, various retrofitting techniques such as the addition of steel plates and concrete jackets with or without fiber-reinforced polymer (FRP) system were implemented (Abdulazeez et al. 2019; Abdulazeez et al. 2019; Stauffer 2016; Wan 2013; Wipf et al. 2003). This report explored two different approaches to repair corroded H-piles. This included using concrete-filled pultruded fiber-reinforced polymer (FRP) tubes and ultra-high performance concrete (UHPC) plates. A brief overview of research on pultruded FRP and UHPC is discussed in the next sections.

1.3 Pultruded FRP

Over the past few decades, strengthening reinforced concrete structures using FRP systems has become widely accepted in the construction industry. Lately, pultruded FRP closed structure shapes also offer new construction potential, mostly when used as a stay-in-place formwork for concrete. One such application involves using concrete-filled FRP tubes (CFPT) as beams or columns for new construction.

Researchers investigated CFPT with different cross-sectional shapes, including circular (Bakis et al. 2002; ElGawady et al. 2010; Fam and Rizkalla 2001; Fam and Rizkalla 2001; Fam and Rizkalla 2002; Mirmiran and Shahawy 1997), rectangular (Belzer et al. 2013; Fam et al.

2005), and square (Ahmed and Masmoudi 2018; Donchev et al. 2019) to understand the response of the CFFT under axial and bending loads.

The FRP tubes can be classified based on the fibers' direction with respect to the structural member. FRP tubes with fibers oriented perpendicular to a structural member to provide concrete confinement were used, in addition to FRP tubes with fibers oriented parallel to a structural member to enhance the tested member's bending stiffness. Most of the studies focused on using pultruded FRP tubes with bi-directional fibers for compression members (Ahmed and Masmoudi 2018; Donchev et al. 2019) and unidirectional fibers for flexural members (Aslani et al. 2019; Fam et al. 2007; Fam et al. 2003; Mohamed and Masmoudi 2010). However, limited studies have been investigated using concrete-filled unidirectional FRP as a compression element.

1.4 Ultra-high Performance Concrete (UHPC)

In research conducted by Farhat et al. (2007), Farzad et al. (2018), and Ichikawa et al. (2016), ultra-high performance concrete (UHPC) has received considerable attention in new construction and repair of infrastructure because of its improved tensile strength, early compressive strength, workability, and durability compared to conventional concrete, as explored in de Larrard and Sedran (1994), Graybeal (2011), Shafieifar et al. (2017), and Wille et al. (2011). UHPC members can reduce the required concrete section depth compared to conventional reinforced or prestressed concrete sections, which reduces the weight of UHPC sections compared to its counterpart sections by up to 70% (Perry 2006).

The characterization of the interface between the H-pile and UHPC under monotonic load remains largely unknown. Studies have been carried out on investigating the bond characteristic of deformed steel bars embedded in UHPC (Bae et al. 2016; Bandelt et al. 2017; Hu et al. 2020).

Results demonstrated that UHPC has a high bond strength with steel bars. Wu et al. (2019) analyzed the interfacial load transfer mechanism between H-pile and steel fiber reinforced conventional concrete using push-out testing. Concrete with steel fibers displayed a relatively higher post-peak bearing capacity compared to the one without steel fibers. There is only a single study that investigated the use of ultra-high performance concrete (UHPC) encasement using push-out tests for the repair of the corroded steel H-pile (Shrestha et al. 2020). Different parameters such as the type of casting of the UHPC, i.e., cast-in-place vs. precast elements, thickness and shape of the UHPC elements, an inclusion of carbon fiber reinforced polymer (CFRP) grid, number and grade of bolts were studied. The experimental work demonstrated the prefabricated UHPC plate with 2.25 in. thickness reinforced by two-layers of the CFRP grid and bolted with steel H-pile was capable of transferring up to 81% of the squash load of the H-pile. The repair method proved to be a promising solution in terms of capacity and cost.

1.5 Bolts and CFRP Grids

Several studies were carried out investigating high-strength bolts' behavior in steel-concrete composite beams. Dallam (1968) investigated the push-out testing of 1/2, 5/8, and 3/4 in. diameter A325 (ASTM A325-66) and A449 (ASTM A449-65) high strength bolts and revealed that the ultimate shear capacity of shear connectors (SCs) increased when increasing the SCs diameter. High strength SCs displayed up to twice higher shear strength than that of the welded headed shear studs. Dedic and Klaiber (Dedic and Klaiber 1984) carried out push-out testing on 3/4 in. A325 high strength bolts, with or without single embedded nuts, and found that the shear capacity of SC would be underestimated when analyzed by the formulae suggested by AASHTO (AASHTO 2010) for headed stud SC. Furthermore, while the AASHTO (2013) and ACI 318 (2014) have provided equations to predict the shear strength of SC embedded in normal strength concrete having compressive strength less than 10 ksi, there are no similar standards for UHPC.

1.6 The layout of the Report

This report includes six chapters. Chapter One presents a brief overview of the problem and literature review. Chapter Two presents the axial and bending behavior of the pultruded FRP tube. Chapter Three presents an experimental work on small and full-scale corroded H-piles repaired using concrete-filled pultruded CFRP tubes attached to the H-piles by shear connectors. Chapter Four presents push-out testing results of H-piles embedded in conventional and UHPC concrete jackets. Chapter Five presents an experimental work of small and full-scale corroded H-piles repaired using UHPC plates attached to the H-piles by shear connectors. Chapter Six summarizes the main conclusions and findings of the research project.

Chapter 2 Axial and Bending Behavior of Pultruded FRP tubes

This chapter presents the experimental results of pultruded FRP tubes subjected to a concentric axial compression and bending test.

2.1 Experimental Program

A total of nineteen specimens were tested under concentric compression and bending. All specimens had 4x4 in. square cross-section with a thickness of 0.25 in.

For the compression specimens, four of them had a variable height of 2, 10, 20, and 30 in. without concrete (fig 2.1(a)), three had a height of 10, 20, and 30 in. with plain concrete filling the tube, and three had the height of 30 in. with reinforced concrete filled the tube (table 2.1; fig 2.1(b)).

Table 2.1 Properties of the compression specimens

	Description	Height (in.)	Concrete Strength (ksi)	Reinforcement
Group A	C1	2	---	---
	C2	10		
	C3	20		
	C4	30		
Group B	C5-P	10	5	---
	C6-P	20		
	C7-P	30		
Group C	C8-R	30	5	4 #3
	C9-R	30		
	C10-R	30		

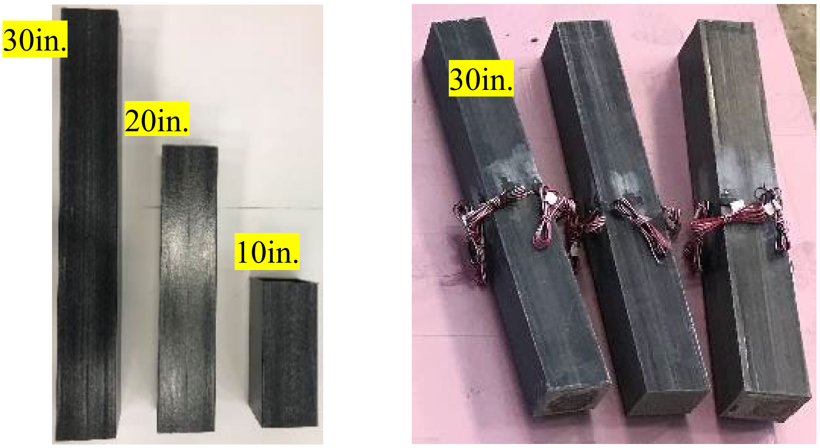

(a) (b)

Figure 2.1 CFPTs: (a) different length parameter, and (b) reinforced tube group

For the bending specimens, three of them had a length of 30 in., three had a length of 30 in. filled with plain concrete, and three had a length of 30 in. filled with reinforced concrete (table 2.2).

Table 2.2 Properties of the bending specimens

	Description	Height (in.)	Concrete Strength (ksi)	Reinforcement
Group A	B1 B2 B3	30	---	---
Group B	B4-P B5-P B6-P	30	5	---
Group C	B7-R B8-R B9-R	30	5	4 #3

The specimens in table 2.1 and 2.2 were labeled as follows: letter C or B indicates a column or beam respectively followed by the number of specimens, letter P indicates plain concrete used in the specimen, while letter R indicates reinforced concrete used.

2.2 Materials

2.2.1 Pultruded FRP

The properties of the FRP tubes are shown in table 2.3. The tensile and compressive properties of the FRP were tested per ASTM D-638 and ASTM D-695 respectively and they were found to be consistent with the properties provided by the manufacturer.

Table 2.3 Properties of FRP as provided by the manufacturer

Property	Typical value
Ultimate tensile strength	30,000 psi
Tensile Modulus	2.5 x 10^6 psi
Ultimate compressive strength	30,000 psi
Compressive Modulus	2.3 x 10^6 psi

2.2.2 Rebars

The reinforcing bars have been designed to withstand a bending moment corresponding to an e/t of 5% at the yield strength of the unfilled FRP tube. However, due to availability and even distributions of the rebar, the bending moment capacity of rebar corresponded to an e/t of 6.22% at a yield strength of the unfilled FRP tube. Four #3 two-leg closed bars with 180 hooks were used. The shape of the bars was selected to ensure there is an adequate development length for #3 bars per ACI-318 (2014).

2.2.3 Concrete

The concrete type used was synthesized using ordinary Portland cement (OPC) type I. The concrete had f'_c of 5 ksi on the day of testing and it has the mix design illustrated in table 2.4.

Table 2.4 Mix Design of the used conventional concrete

Mix	Coarse Agg.	Fine Agg.	Water	Cement	W/C
kg/m^3 (lb./yd^3)	1033 (1742)	1597 (2033)	162 (273)	249 (420)	0.65

2.3 Test Setup and instrumentation

Figure 2.2 shows a 500 kips capacity MTS testing machine that was used for testing the columns. The load was applied monotonically, at a rate of 0.05in./min, until rupture occurred and the test specimen became unstable.

Figure 2.2 Compressive test setup

A four-point bending test was performed over a simple clear span of 27 in. following the ASTM D7250. The load was applied at two points with a load span of 9 in. Figure 2.3 shows the details of the experimental setup. The load was applied using the 500 kips capacity MTS testing machine at a load rate of 0.05in./min.

Eight uniaxial strain gauges were used to measure the strains on the middle of the columns and beams. Two linear variable displacement transducers (LVDTs) were placed at the 1/3 and 2/3 points on the length of the beam to determine the deflection profile of the tested beams.

Figure 2.3 Bending test setup

2.4 Test Results and Discussion

2.4.1 Observed behavior and failure mode

Typical failures of the hollow tubes are shown in Figure 2.4 (a and b). All the hollow tubes failed due to local failure at the end of the tubes, while the concrete-filled tubes all failed because of the rupture of the FRP tube, which occurred at or near the corners.

Typical failures of the hollow tubes are shown in Figure 2.4 (c and d). All the hollow tubes failed due to local failure on the top flange under the loading points, while the concrete-filled tubes all failed because of the rupture of the FRP tube, which occurred at the top corners of the tube.

2.4.2 Effect of tube height

The summary of the experimental results for compression test specimens under Group A is presented in table 2.5. For the effect of the height on the axial capacity of the section, it matched what was predicted since as the height becomes smaller the capacity increased as presented in C1 (2 in. height) figure 2.5(a) where the failure occurred at 98.35 kips with a shortening of 0.076 in. due to local buckling at the edge of the section, while for C2 (10 in. height) figure 2.5(b) the load dropped to 29.09 kips at a shortening of 0.175 in. due to global buckling at the middle of the height. As for C3 (20 in. height) figure 2.5(c), the failure occurred at 48.82 kips at 0.147 in. shortening due to the rupture of the FRP tube at the corners. While for C4 (30 in. height) figure 2.5(d) the failure occurred at 49.49 kips at 0.193 in. shortening due to rapture of the FRP at the corners.

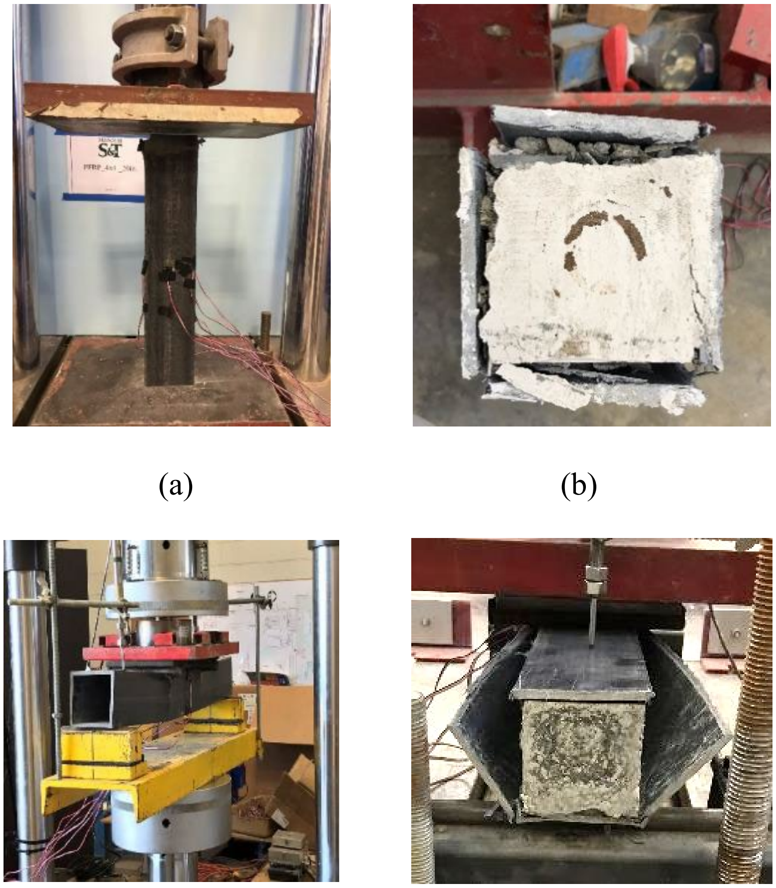

(a) (b)

(c) (d)

Figure 2.4 Failure mode of test specimens (a) hollow columns, (b) concrete-filled columns, (c) hollow beams, (d) concrete-filled beams.

Table 2.5 Test Results of hollow Tube columns with different length

Designation	Height (in.)	Axial Load (kips)	Axial Shortening (in.)
C1	2	98.5	0.08
C2	10	29.0	0.17
C3	20	49.0	0.15
C4	30	49.5	0.20

From the results it is stated that the buckling load for the tested section was 49 kips as no change occurred between the two specimens C3 and C4 where the first one had a 20 in. height and the second one had a 30 in. height and both failed at the same capacity with the same mode of failure.

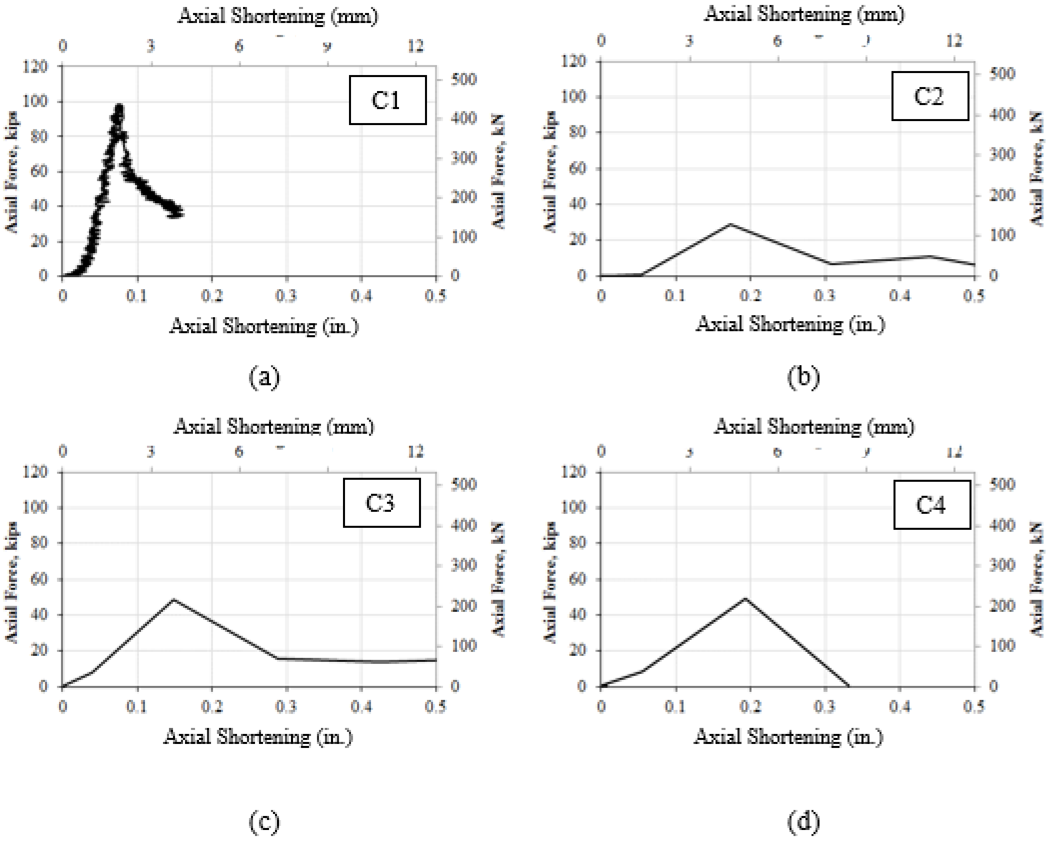

(a) (b)

(c) (d)

Figure 2.5 Axial Load vs axial shortening

2.4.3 Effect of adding concrete

For the compression test specimens, filling the hollow FRP with concrete changed the axial capacities and the failure mode of the tested specimens (table 2.6). For C5-P (10 in. height), as shown in figure 2.6(a), the failure occurred at 112.42 kips at 0.582 in. shortening due to the rapture of the FRP tube at the corners. Similarly, for C6-P (20 in. height), as shown in figure 2.6(b), the axial capacity was 105.6 kips at 0.494 in. shortening due to the rapture of the FRP tube at the corners. As for C7-P (30 in. height), figure 2.6(c) shows the capacity was 95.48 kips at 0.49 in. shortening due to the rapture of the FRP tube at the corners.

Table 2.6 Test Results of concrete-filled tube columns with different length

Designation	Axial Load (kips)	Axial Shortening (in.)
C5-P	112.5	0.58
C6-P	106.0	0.49
C7-P	95.5	0.49

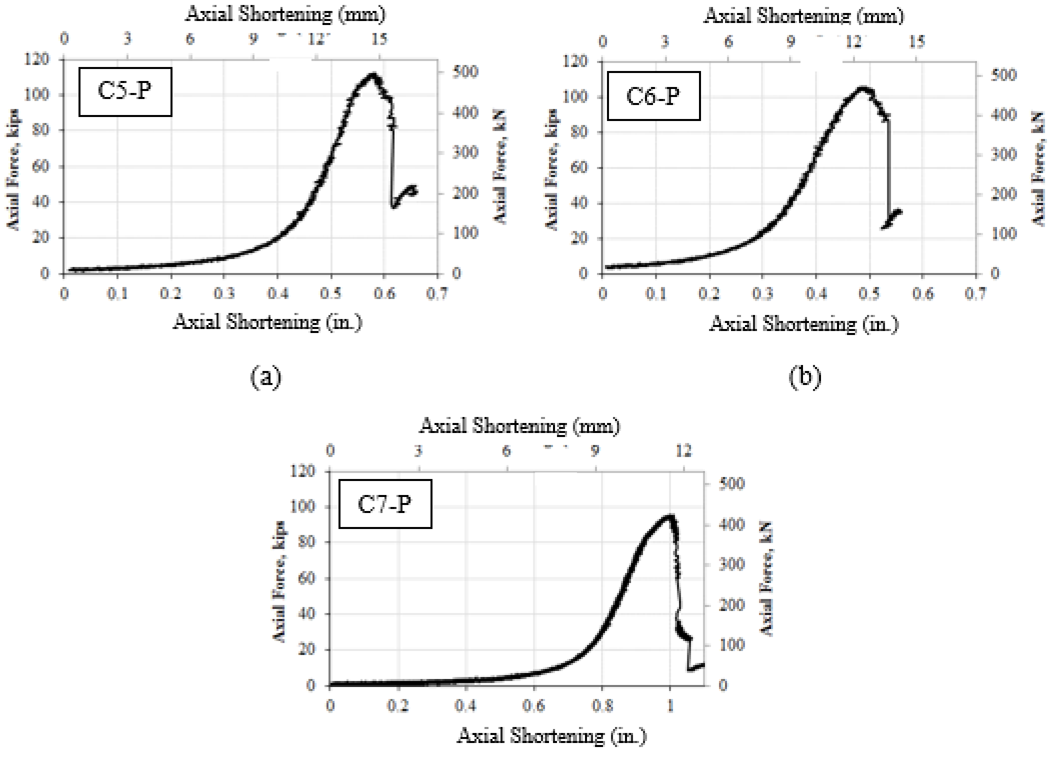

(a) (b)

(c)

Figure 2.6 Axial Load vs axial shortening

Adding the plain concrete to the hollow FRP tube did not change the capacity nor the mode of failure of the lower height of 10 in. as it only increased the load by 14%. While for the bigger heights it increased the capacity by 116% for the 20 in. and by 93% for the 30 in. specimens while the mode of failure changed from local yielding of the FRP tube at the top of the specimens to the rapture of the FRP tube at the corners.

Filling the hollow FRP tube with concrete changed the bending capacities and the failure mode of the bending test specimens (table 2.7). All the tested specimens (B4-P, B5-P, and B6-P) failed nearly at the same load of 18.3, 18.5, and 18.5 kips respectively with deflection varying from 0.4 to 0.51 in. (fig. 2.7). They failed with the same mode of failure; the rapture of the FRP tube at the top corners at the compression side of the beams.

Adding the plain concrete to the hollow FRP beam increased the capacity of the section from 10 kips to 19 kips for a 190% increase in load.

Table 2.7 Test Results of concrete-filled tube beams

Designation	Load kips (kips)	Deflection (in.)
B4-P	18.3	0.40
B5-P	18.5	0.41
B6-P	18.5	0.51

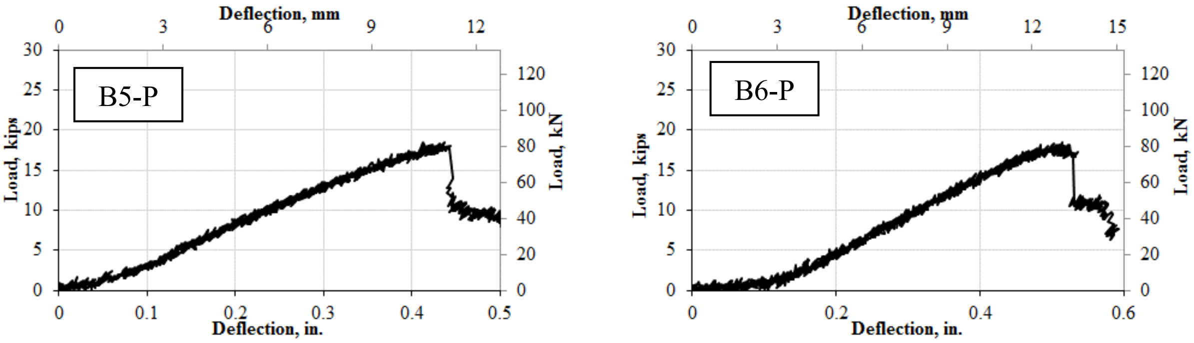

(a) (b)

Figure 2.7 Load vs Deflection

2.4.4 Effect of adding reinforced concrete

In compression test specimens, adding reinforcement to the concrete-filled FRP tube changed the axial capacities but did not change the failure mode of the tested specimens (table 2.8). All the tested specimens (C8-R, C9-R, and C10-R) failed nearly at the same load of 75.0, 82.0, and 82.3 kips respectively with deflection varying from 0.18 to 0.25 in. (fig. 2.8) with the same mode of failure which is the rapture of the FRP tube at the corners. Adding reinforcement to the plain concrete in the hollow FRP columns decreased the capacity of the section from 95.48 kips to 79.7 kips for a 17% decrease in load. Adding the reinforcement to the plain concrete in the hollow FRP tube changed the capacity but didn’t change the mode of failure.

Table 2.8 Test Results of reinforced concrete-filled tube columns

Designation	Axial Load (kips)	Axial Shortening (in.)
C8-R	75.0	0.25
C9-R	82.0	0.22
C10-R	82.3	0.18

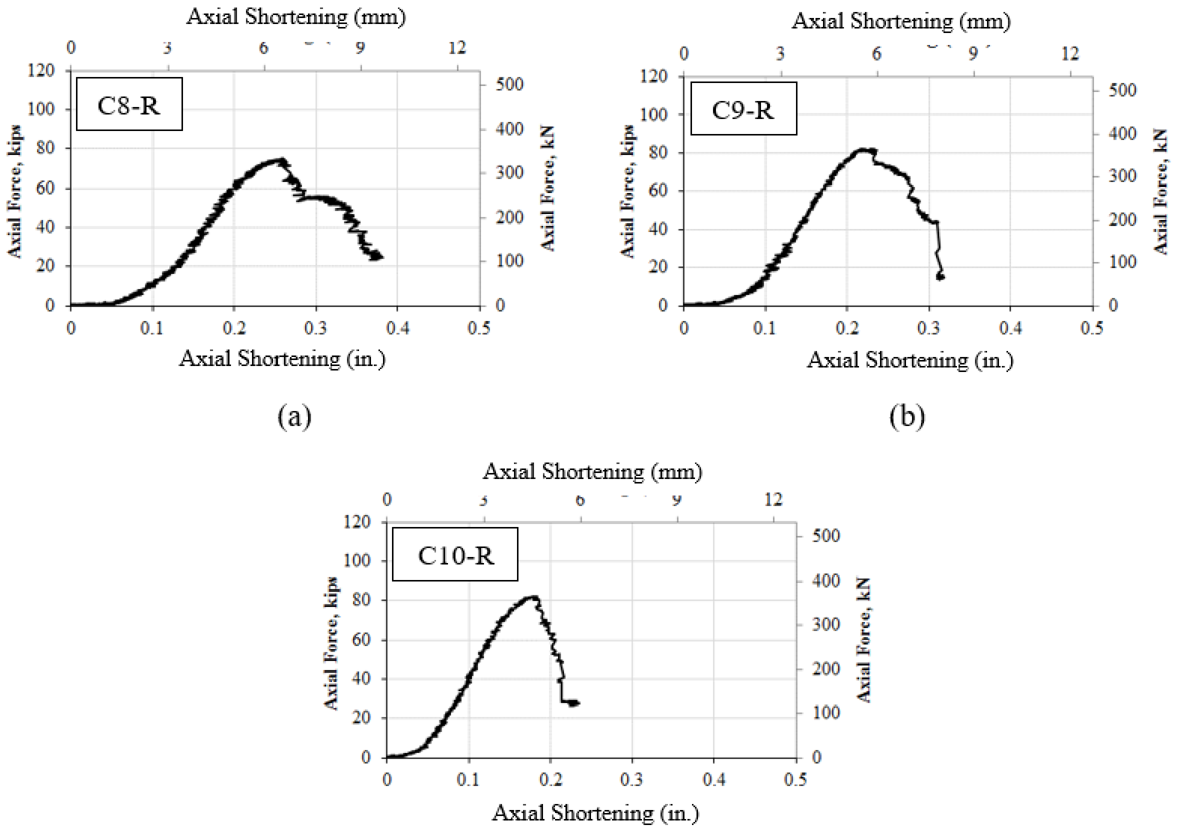

(a)

(b)

(c)

Figure 2.8 Axial Load vs axial shortening

In bending test specimens, adding reinforcement to the concrete-filled FRP tube changed the bending capacities without changing the failure mode of the tested specimens (table 2.9). All the tested specimens (B7-R, B8-R, and B9-R) failed nearly at the same load of 29.5, 30.05, and 27.69 kips respectively with deflection varying from 0.382 to 0.52 in. (fig. 2.9) with the same mode of failure; the rapture of the FRP tube at the top corners at the compression side of the beams.

Table 2.9 Test Results of reinforced concrete-filled tube beams

Designation	Load (kips)	Deflection (in.)
B7-R	24.0	0.37
B8-R	30.0	0.53
B9-R	27.7	0.49

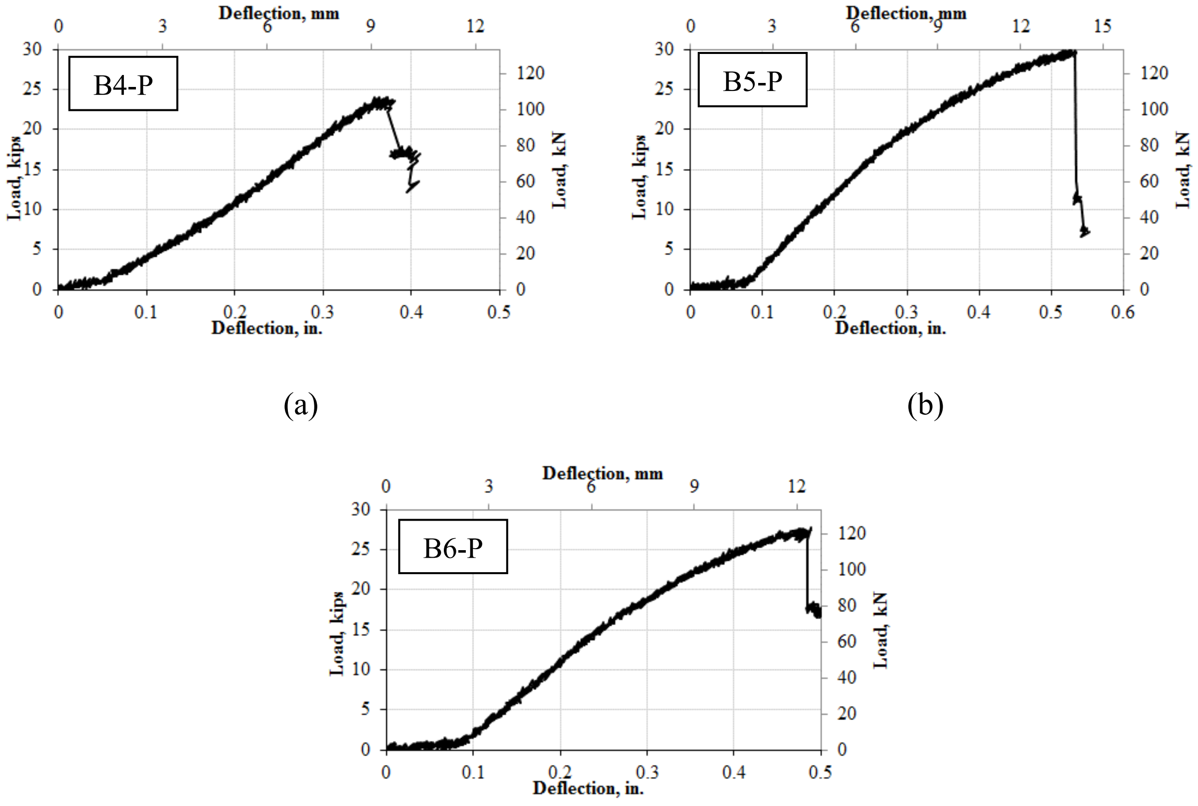

(a)

(b)

(c)

Figure 2.9 Load vs Deflection

Adding reinforcement to the plain concrete in the hollow FRP beam increased the capacity of the section from 18.5 kips to 29.5 kips for a 60% increase in the load of the unreinforcement concrete-filled FRP tube and a 195% increase in the axial capacity of the hollow FRP tube.

2.4.5 Comparison of Experimental and Analytical Models

ACI-440-2R (2017), adopted equation 2.1 to calculate the nominal axial strength of non-prestressed FRP members filled with concrete, as a function of the compressive strength of confined concrete, f'_{cc}, a gross sectional area of concrete, A_g, specified yield strength of non-prestressed steel reinforcement, f_y , and the total area of longitudinal reinforcement, A_s.

$$P_n = 0.8\left[0.85 f'_{cc}\left(A_g - A_s\right) + f_y A_s\right] \tag{2.1}$$

The design approach considers the contribution of fibers on the compressive strength based on the compressive strength of confined concrete with the steel reinforcement's contribution.

Table 2.10 presents the calculated axial capacities of the tested specimens, P_n, using the analytical models as well as the ratio of the peak load to P_n. The analytical model was accurate in predicting the strengths of the unreinforced CFPTs while it over-predicted the strengths of the reinforced CFPTs. The peak strengths measured during the experimental work ranged from 0.90 to 1.02 and 0.68 to 0.69 of those predicted using ACI-440-2R (ACI 2017).

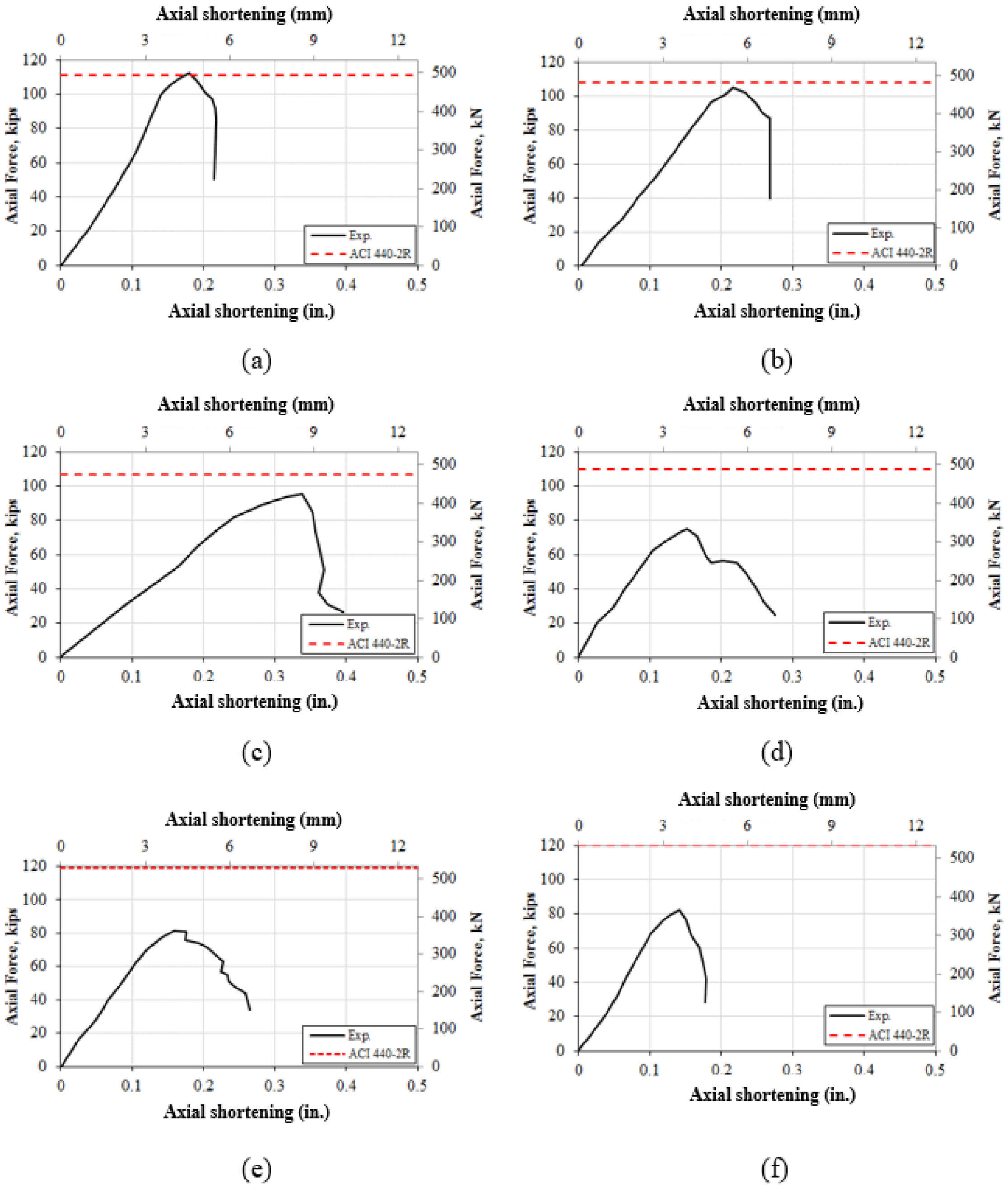

(a)

(b)

(c)

(d)

(e)

(f)

Figure 2.10 Axial force shortening relation: (a) C5-P, (b) C6-P, (c) C7-P, (d) C8-R, (e) C9-R, and (f) C10-R

Table 2.10 Analytical Evaluation of the Axial Capacity of the Tested Specimens

Group	Designation	$P_{exp.}$ (kips)	ACI 440.2R	
			P_n (kips)	$P_{exp.}/P_n$
A	C5-P	113	111	1.02
	C6-P	106	108	0.98
	C7-P	96	107	0.90
B	C8-R	75	110	0.68
	C9-R	82	119	0.69
	C10-R	82	120	0.68

Chapter 3 Behavior of Steel Piles Repaired Using Concrete Filled Pultruded FRP Tubes

This chapter presents the experimental results of two phases during the development of a repair method for corroded H-piles using concrete-filled pultruded CFRP tubes (CFPTs). In Phase I, the behavior of concrete-filled pultruded CFRP tubes (CFPTs) was investigated under a push-out testing to determine the interface shear force that can be transferred between CFPTs and H-piles using different numbers of shear connectors (SC). In Phase II, three corroded H-piles were repaired using the optimized CFPTs system and were tested under concentric axial compression force. These corroded H-piles were tested previously under axial compression and were then straightened, repaired using the CFPTs, and retested under axial loads.

3.1 Experimental Program

The experimental program consisted of the following two phases.

3.1.1 Phase I: Push-out Testing

The test program for Phase I: Push-out Testing of concrete-filled pultruded CFRP (CFPT) specimens is given in table 3.1. The CFPTs of different cross-sections were attached to 10x42 steel H-piles using shear connectors (SC) (fig. 3.1).

Table 3.1 Push-out Test during CFPT-Phase I

Description	Height (in.)	No. of tubes	Dimensions of the tube section (in.)	SC No.	SC Layers Arrangement	Concrete Strength (psi)
CFPT -1T-4SC-2L	10	1	8x4	4	2	5,000
CFPT -2T-4SC-2L		2	4x4	4	2	
CFPT -2T-6SC-3L		2	4x4	6	3	

The specimens in table 3.1 were labeled as follows: CFPT followed by #B, indicating the configuration of the tube, #SC, indicating the number of SCs used, and #L, number of layers of SC.

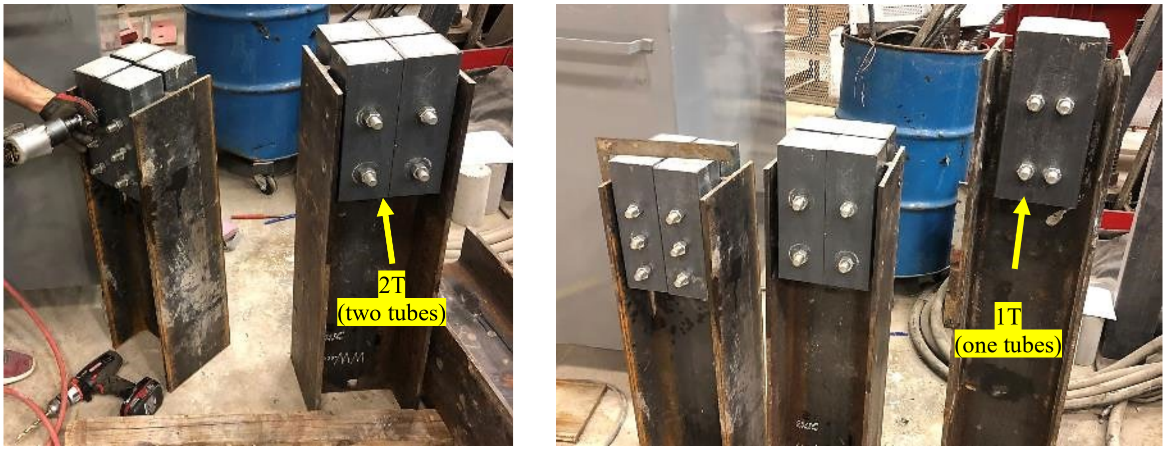

Figure 3.1 CFP-CFRP specimens attached to H-piles

3.1.2 CFPT-Phase II: Large-scale Repair System

The test program for Phase II: Large-scale testing of 120 in. long corroded 10x42 steel H-piles repaired with concrete-filled pultruded CFRP (CFPT) specimens under concentric axial compression force is given in table 3.2. The corroded steel H-piles selected for Phase II are W70-F50/0, W70-F50, and W70-F50-10%. These steel H-piles were previously tested during the assessment task and were reused in Phase II after straightening them.

Table 3.2 Full-scale Repair of the H-piles in CFPT-Phase II

Description	Height in.	CFPT Boxes	CFPT Cross-section (in.)	SC No.	SC layers Arrangement	Concrete Strength (psi)
CFPT -1T-8SC-2L	32	1	8x4	8	4	5,000
CFPT -2T-8SC-2L		2	4x4	8	4	
CFPT -2T-12SC-3L		2	4x4	12	6	

The specimens in table 3.2 were labeled as follows: CFPT followed by #T, indicating the number of tubes on each web, #SC, indicating the number of the SC used, and #L, number of layers of SC.

3.2 Material Properties

3.2.1 H-pile

The material properties such as yield strength, ultimate strength, and modulus of elasticity of HP10x42 a steel H-pile were determined by using a tension test per ASTM E8/E8M-

16a (ASTM-International-E8/E8M-13 2013) on three coupons, cut from each of the flanges and web. The mechanical properties of the steel H-pile are shown in table 3.3.

Table 3.3 Mechanical Properties of H-pile Flange and Web

	Yield Stress (ksi)	Ultimate stress (ksi)	Modulus of Elasticity (E) (10^3 ksi)
Flange	47	75	26.25
Web	59	73	26.40

3.2.2 Pultruded CFRP tube

Two different pultruded tube sections with lengths of 8x4 in. and 4x4 in. and each having a thickness of 0.25 in. were used during this chapter. Different tube lengths ranging from 10 in. to 32 in. were employed during the different phases of this task (tables 3.1 and 3.2). The tensile and compressive properties of the pultruded CFRP are given in table 2.3 of Chapter 2.

3.2.3 Shear Connectors (SC)

Shear connectors (SC) of ASTM A325 heavy hex structural bolts with a minimum tensile strength of 120 ksi and a diameter of 0.75 in. were used to attach the CFPTs to the H-piles using heavy hex nuts.

3.3 Test Setup and Instrumentation

In phase I, an MTS universal testing machine (UTM) of capacity 560 kips was used to perform the push-out test of CFPTs attached to the steel H-pile (fig. 3.2). Each specimen was placed inside the MTS on a rigid steel base. A swivel plate was placed on top of the steel H-pile to transfer the load from the actuator to the specimen, forming a top-pin and bottom hinge boundary condition. Two linearly variable displacement transducers (LVDTs) were vertically installed on top of the CFPTs at the H-pile web to measure their relative axial displacement (fig.

3.2). The load was applied monotonically at a rate of 0.05 in./min until the test specimen ruptured. Each specimen was aligned in both the horizontal and vertical planes to minimize the accidental eccentricity.

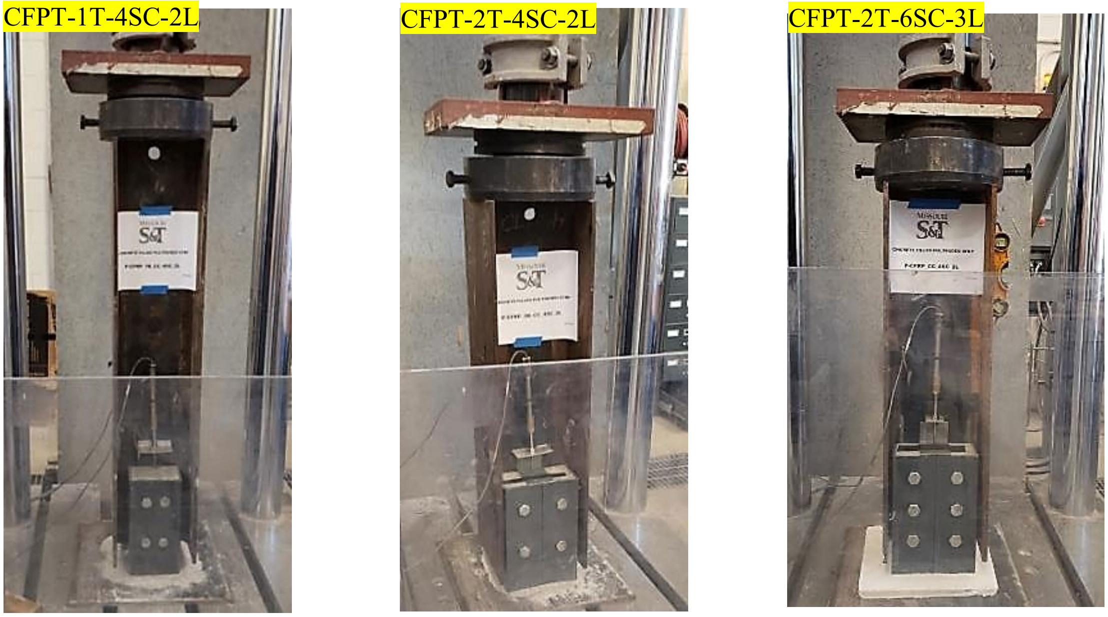

Figure 3.2 Push-out test setup

In Phase II, a self-sustained testing frame (SSTF) of capacity 1,000 kips was used for testing the steel H-pile repaired with CFPTs under axial compression. The SSTF consists of two exterior rigid red beams and one movable black beam. The two rigid red beams are connected by six DYWIDAG bars with a grade of 150 and diameter of 1.375 in. Six 200 kips load cells were placed on the six DYWIDAG bars to monitor the applied load. The axial force was measured as the sum of the values of the load cells installed on the bars. The movable black beam resting on four rollers is guided using unidirectional movement on two rail tracks.

Each end of the test specimen was placed inside a steel toe connected to a half-sphere. The test specimen was then placed inside the SSTF in between the red beam and black beam so that each end of the half-spheres were inside swivel plates attached to the exterior red beam and the black beam. This formed a pin-pin boundary condition. The load was applied monotonically using hydraulic jacks, each having 500 kips, at a rate of 35 kips/min using an oil pump until rupture occurred and the test specimen became unstable.

Forty-eight strain gauges were attached to each H-pile specimen's web and flanges to measure the axial strains. Two string-potentiometers were attached between the movable beam and the rigid beam next to each specimen. Additional five string-potentiometers were installed to measure the displacements of each H-pile in the horizontal direction and three string pots to measure the vertical displacement.

Figure 3.3 Large scale test setup

3.4Results and Discussion

3.4.1 Phase I: Push-out Testing

Table 3.4 shows the push-out test results of CFPT specimens and their failure modes. The push-out testing showed catastrophic failures with splitting failure occurring along the tube corners. The failure often occurred at the bottom corners that were in contact with the webs.

Figure 3.4 displayed the specimens after push-out testing, and figure 3.5 shows the axial force versus displacement.

Table 3.4 Push-out Test Results

Test specimens	Peak Load (kips)	Displacement (in.)	Failure Mode
CFPT -1T-4SC-2L	141.8	0.30	CFRP rupture at corner
CFPT -2T-4SC-2L	125.7	0.24	Splitting of CFRP and concrete
CFPT -2T-6SC-3L	177.2	0.25	Splitting of CFRP and concrete

Figure 3.4a shows the failure mode of specimen 1T-4SC-2L, dominated by the rupture of CFPTs at the corners right next to the web of the H-pile. The CFPT rupture proceeded by splitting initiating at the tube corners due to the stress concentration because of the concrete fill lateral expansion. Beyond that, debonding occurred between the filled concrete and the CFPTs until the specimen's failure. It reached an ultimate axial capacity of 141.8 kips and the highest axial shortening of 0.3 in. (fig. 3.5a), compared with the shortening of the other two specimens, 2T-4SC-2L and 2T-6SC-3L.

Figures 3.4b and 3.4c show the failure modes of the specimens 2T-4SC-2L and 2T-6SC-3L, respectively, which were mainly splitting failure initiating at both the concrete and CFRP and observed along the longitudinal direction passing through the center of the SCs. The peak load was 125.7 kips for 2T-4SC-2L (fig. 3.5b) and 177.2 kips for 2T-6SC-3L (fig. 3.5c).

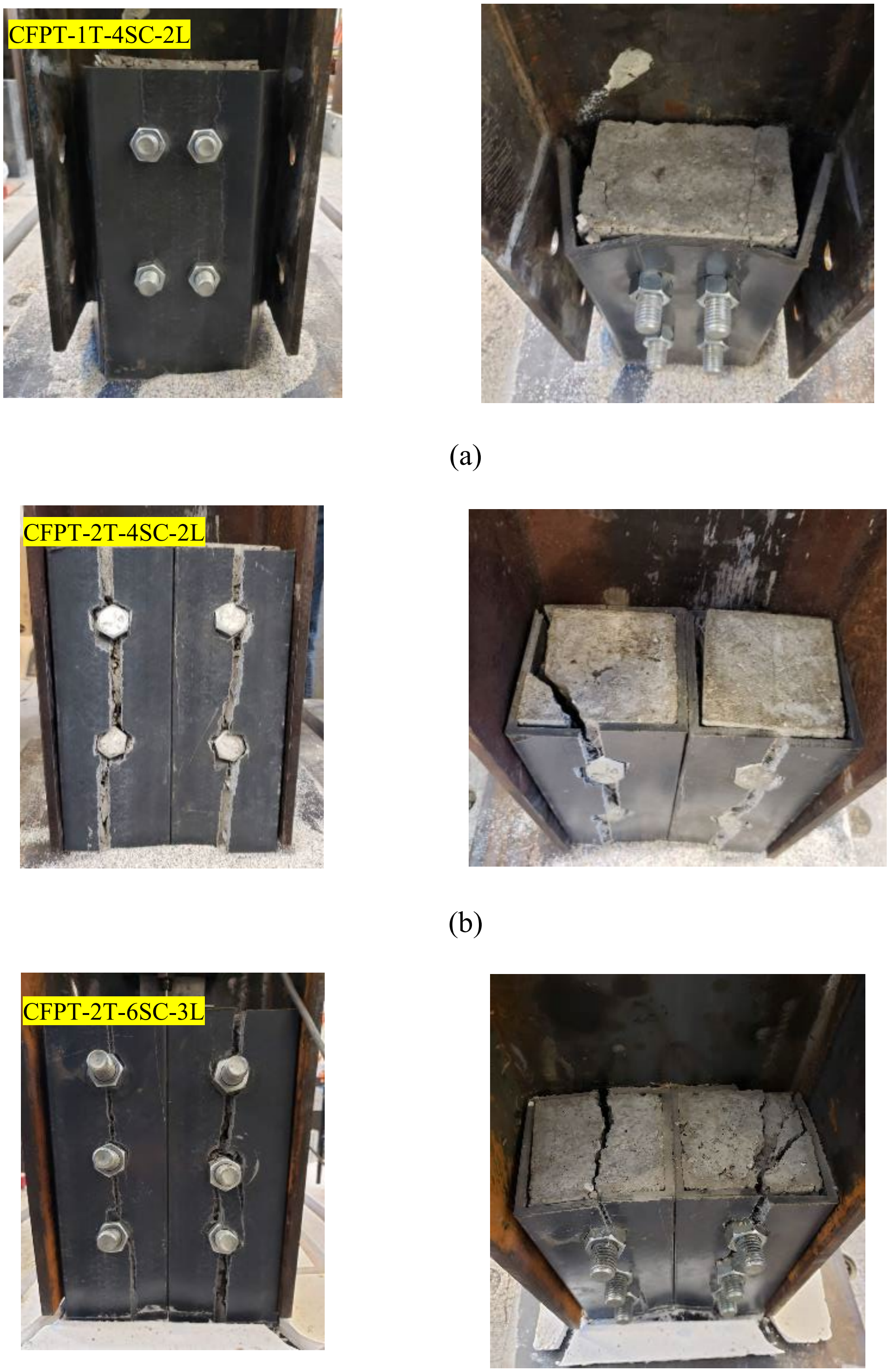

(a)

(b)

(c)

Figure 3.4 Failure modes of push-out tested specimens: (a) CFPT-1T-4SC-2L, (b) CFPT- 2T-4SC-2L, and (c) CFPT-2T-6SC-3L

The shear transfer increased by 41% as the number of SCs increased by 50% from 4SC to 6SC. This was attributed to the addition of two additional SCs along with an extra layer that reduced the stress concentration around the SCs. However, there was no significant difference in the axial shortening between the two specimens.

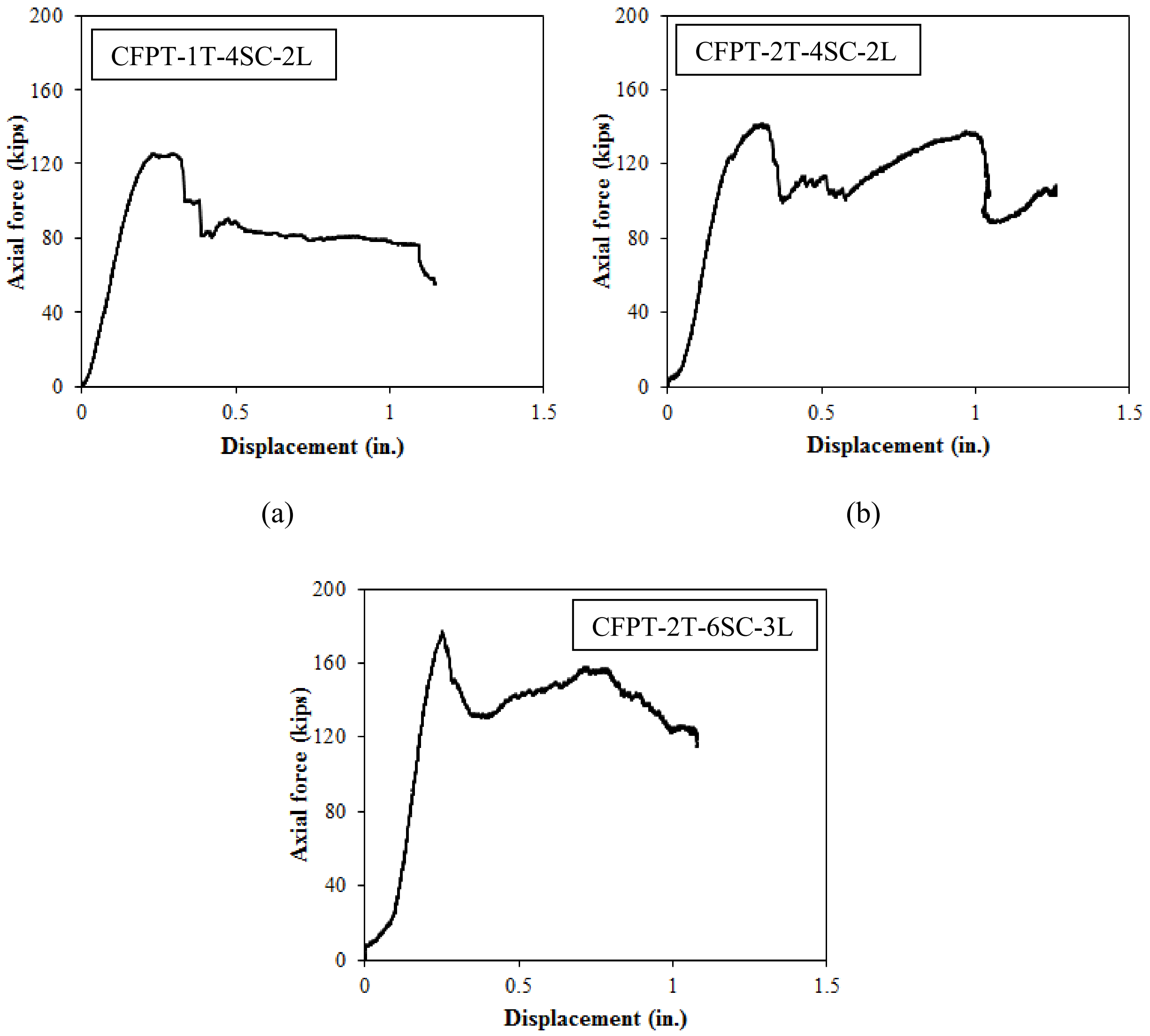

(a) (b)

(c)

Figure 3.5 Axial force versus displacement curve (a) CFPT-1T-4SC-2L, (b) CFPT- 2T-4SC-2L, and (c) CFPT-2T-6SC-3L

3.4.2 CFPT-Phase II: Large-scale Repair System

Table 3.5 shows the results of large-scale testing of the steel H-pile repaired with CFPT under compression and it’s failure modes. Figure 3.6 shows CFPT specimens before and after the testing. The failure mode was dominated by the global buckling at the corroded section location. Moreover, increasing the SC number used to attach the CFPTs improved the repaired-after-corrosion H-pile in terms of the axial capacity (table 3.5). In all three specimens, the failure mode was a global buckling, as anticipated by obtaining the same buckling shape during testing of the original corroded H-piles. However, the axial load and shortening at the failure were different.

Table 3.5 Summary Results of Tested Full-scale Repaired H-piles

ID	Specimen Name	Steel H-piles	CFPT No.	SC No.	Unrepaired Axial Capacity (kips)	Repaired Axial Capacity (kips)	% Decrease
R1	CFPT -1T-8SC-2L	W70-F50/0	1	8	278	102	63
R2	CFPT-2T-8SC-2L	W70-F50	2	8	280	139	50
R3	CFPT-2T-12SC-3L	W70-F50-10%	2	12	223	190	21

In specimen R1 (table 3.5), the corroded H-pile was repaired with one CFPT on each web and eight shear connectors(SC) that were distributed over two layers with two SCs per layer. The test results revealed the lowest failure axial load of 102 kips and the highest axial shortening of 0.90 in. compared to the other tested specimens (fig. 3.7a). Increasing the number of CFPTs to two and keeping the other parameters similar to those used in specimen R1 resulted in an increase in the axial failure load to 139 kips and a decrease in the axial shortening to 0.65 in (fig. 3.7b).

In specimen R2 (table 3.5), the corroded H-pile was repaired with two CFPTs on each web and eight shear connectors (SC) distributed over two layers with two SCs per layer. The axial capacity of the R2 specimen increased by 29%, and shortening decreased by 28% compared with the R1 specimen. This could be explained by the two extra pultruded tubes' webs, which increased the specimen's stiffness and delayed the debonding between the PFRP and concrete.

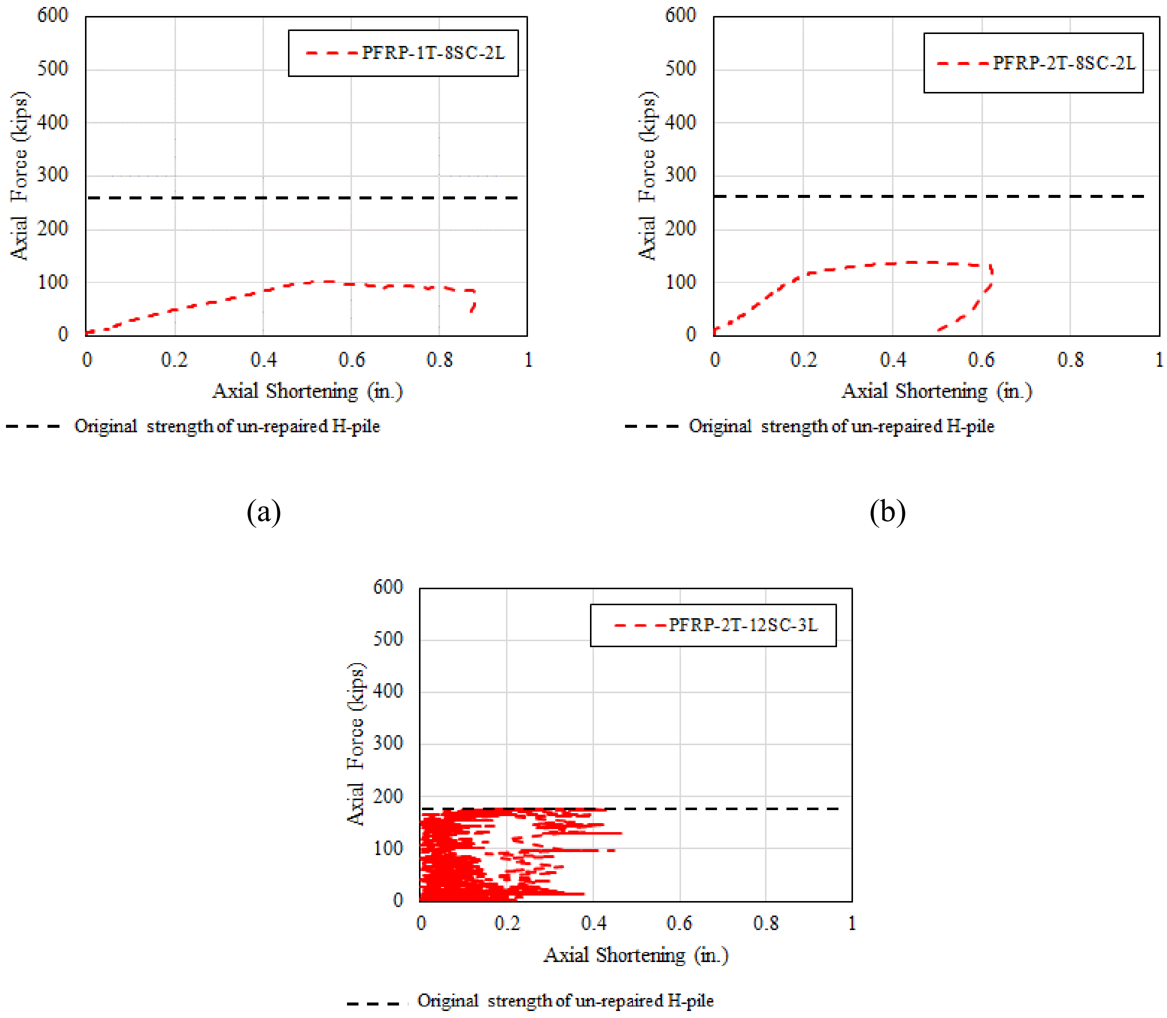

(a) (b)

(c)

Figure 3.6 Axial force versus axial shortening of large-scale repaired H-pile (a) CFPT-1T-8SC-2L, (b) CFPT-2T-8SC-2L, and (c) CFPT -2T-12SC-3L

In the case of specimen R3, the corroded H-pile was repaired with two CFPTs on each web and twelve shear connectors (SC) distributed over three layers with two SCs per layer. Increasing the number of SC in the specimen R3 to twelve distributed over three layers while keeping other parameters (i.e., CFPTs configuration) similar to that of R2 resulted in the highest failure axial load at 190 kips and the lowest axial shortening of 0.40 in. compared to the other specimens (fig. 3.7c). The axial load increased by 41% while the shortening decreased by 38%

compared with the R2 specimen. Adding two extra SCs reduced the FRP tubes' buckling length at the compression side resulting in a higher failure axial load and stiffness of the corroded section.

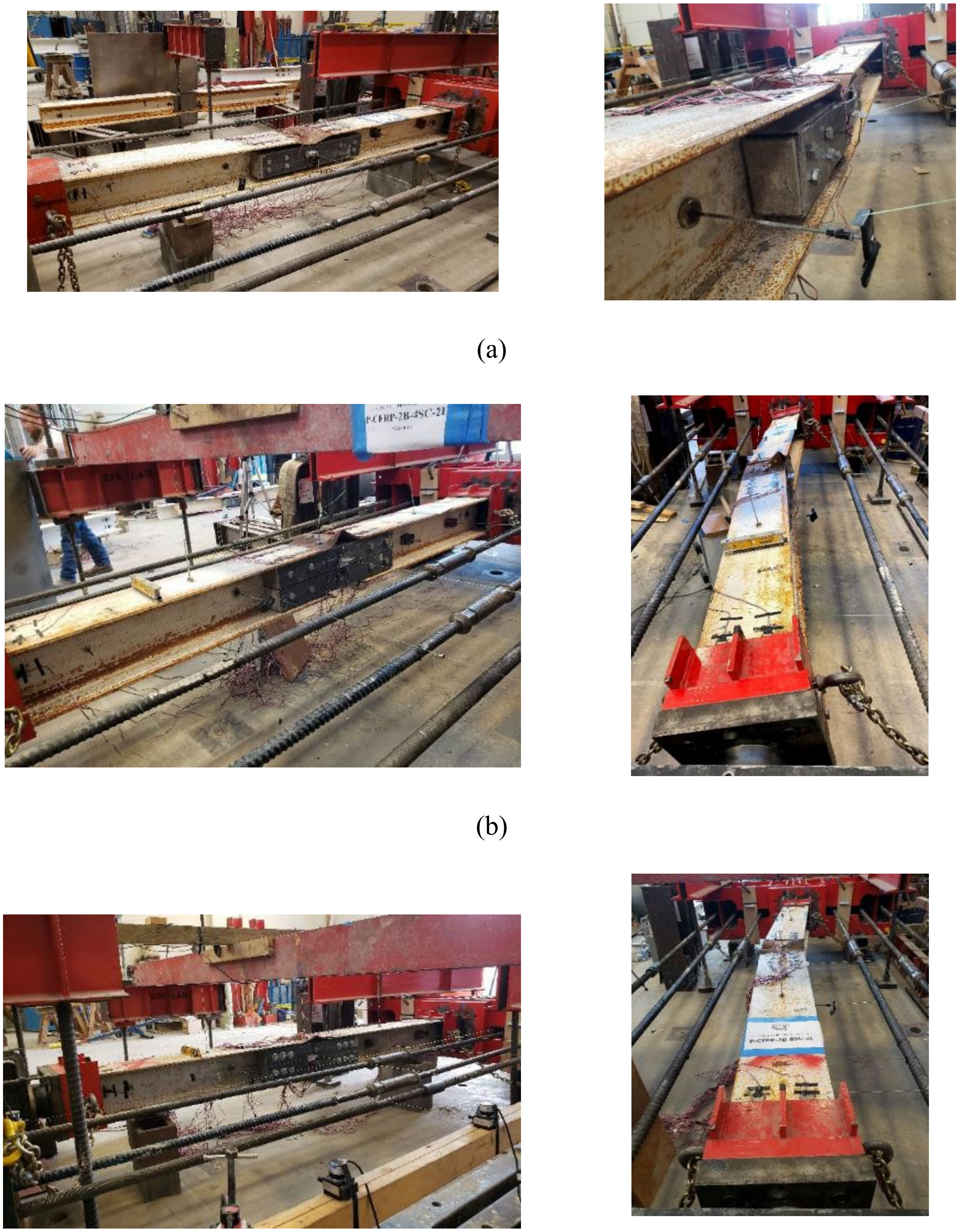

(a)

(b)

(c)

Figure 3.7 Large-scale repaired H-pile before and after the test: (a) CFPT-1T-8SC-2L, (b) CFPT-2T-8SC-2L, and (c) CFPT-2T-12SC-3L

Chapter 4 Interfacial Bond Strength between H-piles and Different Concrete Jackets

This chapter presents the experimental results of push-out tests carried out on six steel H-piles encased by different types of concrete jackets. Ultra-high performance concrete (UHPC) and conventional concrete (CC) were used as different concrete jacket types. Three different embedment lengths were used for each concrete type specimen. The interfacial bond behavior between the steel H-pile and concrete encasement was investigated under the push-out test.

4.1 Experimental Program

A total of six specimens were subjected to push-out tests to examine the bond strength for different concrete encasement jackets (table 4.1). For all specimens, the 10x42 steel H-pile was encased by a cylindrical concrete jacket of diameter 20 in. for up to three different embedment lengths, L_e, of 2.5 in., 5.0 in., and 7.5 in. (fig. 4.1).

Table 4.1 Parametric Study

Group	Specimen Name	Concrete Type	f'_c (ksi)	Concrete Jacket Length, L_e (in.)
A	U1	UHPC	15.5 ±0.2	2.5
	U2			5.0
	U3			7.5
B	C1	CC	5.1 ±0.2	2.5
	C2			5.0
	C3			7.5

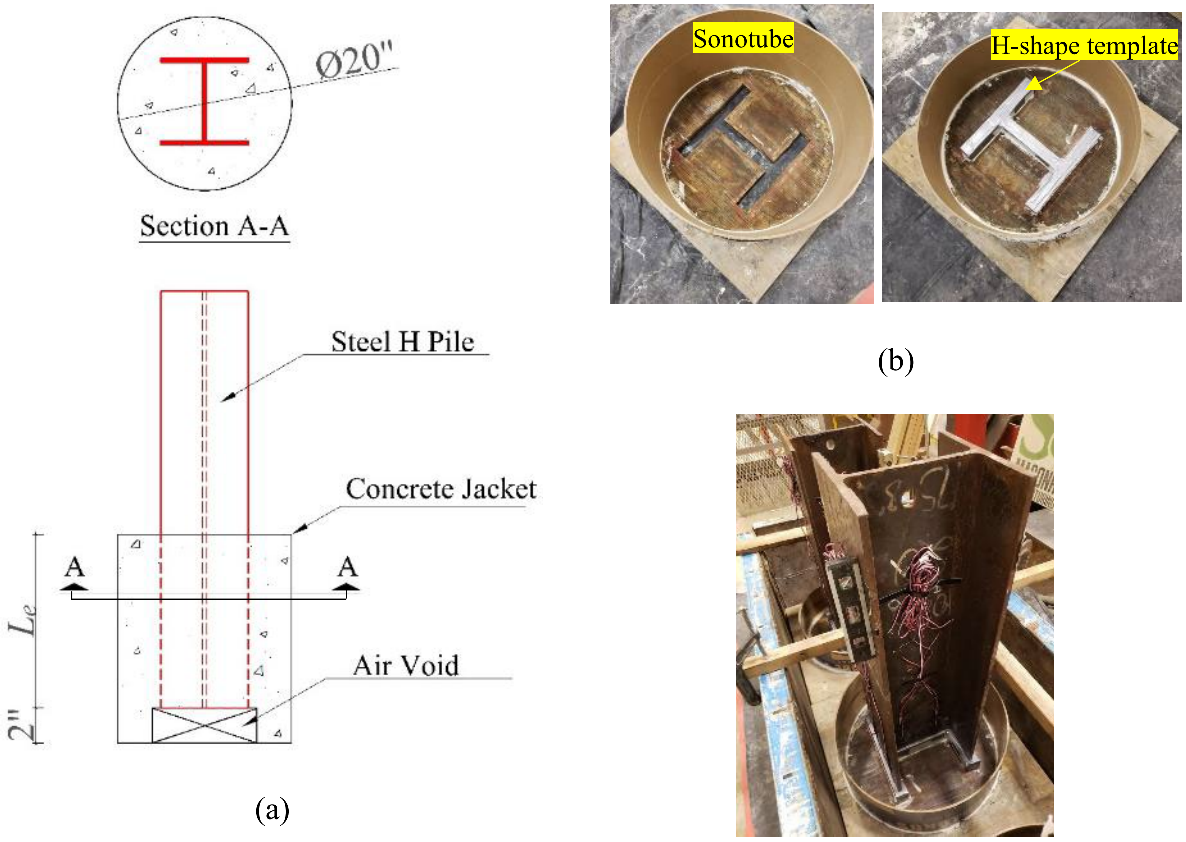

(a)

(b)

(c)

Figure 4.1 Specimen preparation: (a) layout (b) H-shape template (c) placing H-pile on the template

The specimens in table 4.1 were labeled as follows: letter U or C indicate UHPC jacket or conventional concrete jacket respectively followed by number designating the L_e value as multipliers of 2.5 in. (e.g., 2 stands for Le of 5.0 in.).

4.2 Material Properties

4.2.1 H-pile

The mechanical properties of steel H-piles for this chapter are the same as specified in table 3.3 of Chapter 3.

4.2.2 Ultra-high Performance Concrete (UHPC)

Nonproprietary ultra-high performance concrete (UHPC) was developed as shown in table 4.2 and adopted in this study. The UHPC was prepared using high early strength Portland cement type III, ground granulated blast furnace slag, fine dry sand, and water. Polycarboxylate high range water reducer (HRWR), having a solid mass content of 23%, was used to enhance the UHPC workability. Straight 0.0079 in. diameter and 0.51 in. long micro steel fibers were used, at a volume fraction of 2% of the UHPC volume, to improve ductility and minimize the tensile cracks. The tensile strength and elastic modulus of the steel fiber were 275.57 ksi and 29,442.7 ksi.

The UHPC mixing was initiated by blending the fine sand and steel fibers into a high shear mixer for two minutes, followed by gradually adding and mixing about 50% of the total water for another two minutes (fig. 4.2). After that, the cementitious materials were added and mixed for three minutes. The remaining water, mixed with HRWR, was added, and the mixing was continued for another eight to ten minutes. The homogenous UHPC displayed a mini-slump flow spread test, per ASTM C1437 (ASTM-C1437 2007), ranging from 10 in. to 12 in..

Table 4.2 Mixture Design of the UHPC

w/c*	Cement Type III (lb/yd^3)	Slag (lb/yd^3)	Fine Sand (lb/yd^3)	HRWR (lb/yd^3)	Water (lb/yd^3)	Steel Fiber (lb/yd^3)
0.2	1,593	371	1,699	73.8)	337	265

**Ratio of the total liquid (water content in HRWR and water) to the cementitious materials (cement and slag).*

4.3 Test Specimens Preparation

Table 4.3 presents geometrical properties of the steel H-pile and concrete jackets used and fig. 4.1a shows the layout of concrete-encased steel H-pile specimen. Sonotube of diameter 20 in. was glued to a wooden base, having an H-shaped template at its center (fig. 4.1b).

Table 4.3 Specimen Geometrical Properties

H-pile	Concrete Encasement		
Section	Configuration	Contact Perimeter (*p*) (in.)	Diameter (*D*) (in.)
10 × 42	Cylinder	59.0	20

A 2 in. high H-shaped form was placed in the template (fig. 4.1b) and the steel H-pile was placed on the form, forming a gap inside the concrete jacket underneath the H-pile specimen (fig. 4.1c). This gap was provided to allow the H-pile to slip downward freely during testing.

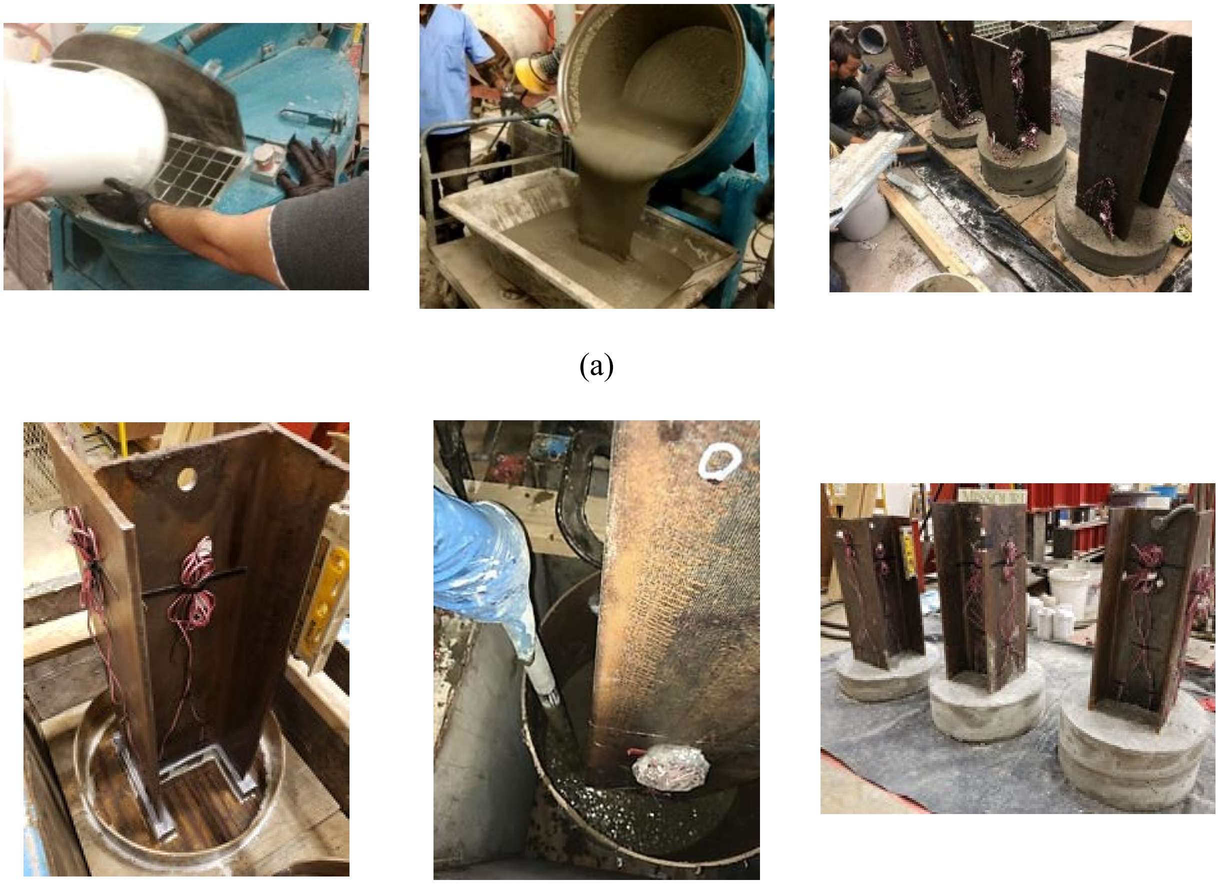

(a)

(b)

Figure 4.2 Concrete encasement placing (a) UHPC, and (b) CC

4.3.1 Concrete Encasement Casting and Curing

The homogenous UHPC was placed inside the Sonotube® giving a cylindrical concrete jacket shape (fig. 4.2a). Several 2 in. standard cubes and 4 x 8 in. cylinders were also cast. During casting, no mechanical vibrators or tamping rods were used. After casting, the concrete jacket specimens, cubes, and cylinders were covered with plastic sheets to prevent moisture loss and were demolded after 24 hours of placing the UHPC.

The CC mixing, and placing (fig. 4.2b) was carried out as per ASTM C192-16 (ASTM-C192/C192M-16 2016). Several 4 x 8 in. cylinders were also cast. During casting, mechanical vibrators and tamping rods were used. After casting, the specimens were covered with plastic sheets to prevent moisture loss and were demolded after two days. Then, the concrete jacket specimens and cylinders were covered with wet burlap sheets and cured at an ambient temperature of 23 ± 2 °C (73 ± 3 °F). The cylinders were tested periodically during the curing period. Once the target compressive strength was reached, the curing was stopped, and the specimens were tested.

4.4 Test Set-up and Instrumentation

The UHPC or CC encased steel H-piles were tested under push-out testing using MTS universal testing machine. The test setup is the same as described in Section 3.1.1 of Chapter 3. Electrical strain gauges were mounted on the web and flanges of the steel H-piles before placing the concrete jacket to measure the axial strain distributions during the test (fig. 4.3b). The strain gauges were arranged at cross-sections 2.5 in. apart on average, with the first section located 1.25 in. from the free edge of the pile and extending along the embedded length of each jacket. Seven strain gauges were distributed at each horizontal cross-section (fig. 4.3b). The slip between the concrete jacket and steel was also measured using two linear variable displacement transducers (LVDTs) that were placed vertically, at a 3.0 in. gauge length, on the flanges of the steel piles (fig. 4.3c-d).

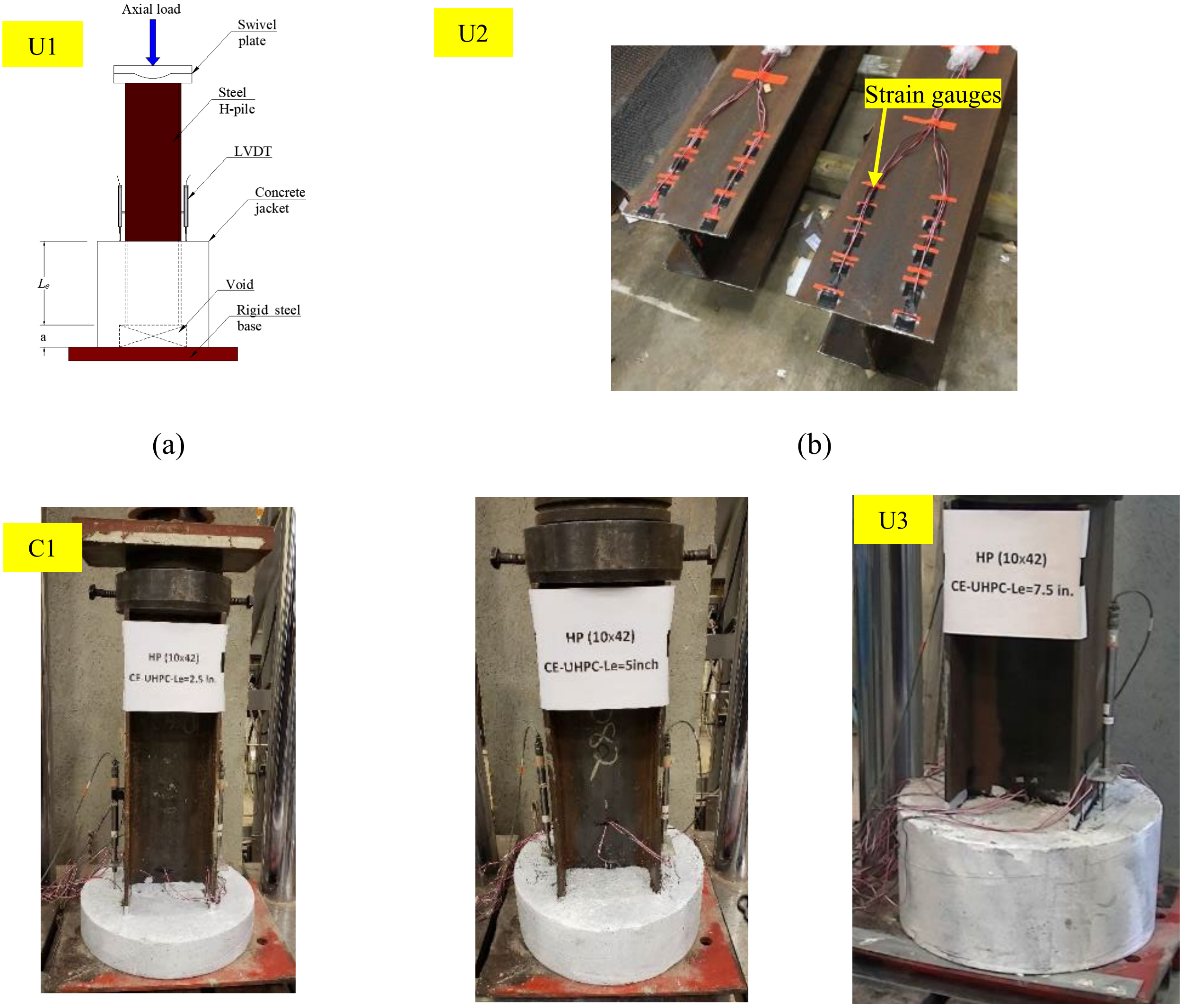

(a) (b)

(c)

Figure 4.3 Instrumentation of the test specimens (a) test layout, (b) strain gauges mounted on the H-pile, (c-d) LVDTs mounted on flanges of an H-pile with UHPC, and CC specimens

(d)

Figure 4.3 cont. Instrumentation of the test specimens (a) test layout, (b) strain gauges mounted on the H-pile, (c-d) LVDTs mounted on flanges of an H-pile with UHPC, and CC specimens

4.5 Results and Discussion

Figure 4.4 displays the bond stress versus the slip of the tested specimens.

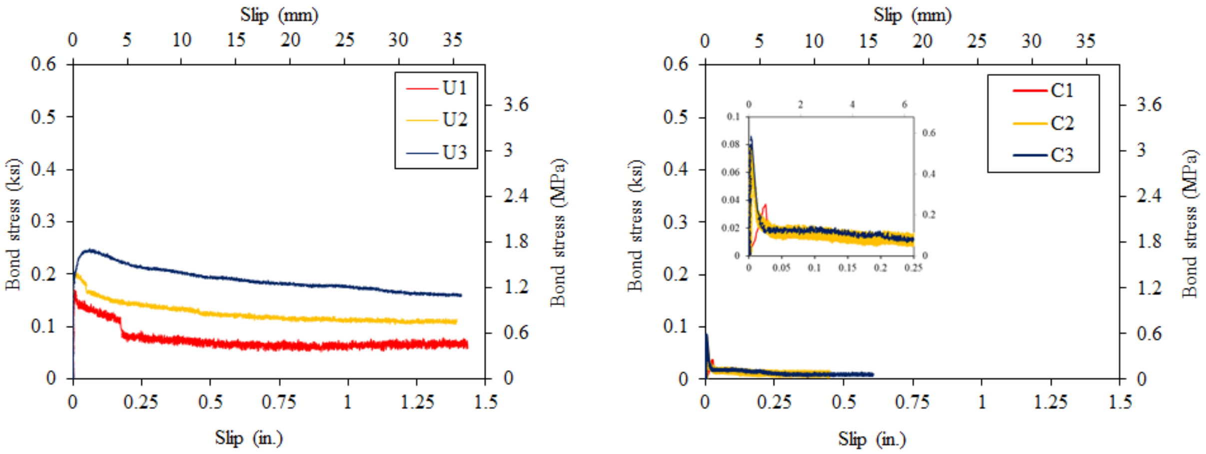

(a) (b)

Figure 4.4 Typical bond strength versus slip of tested specimens (a) UHPC, and (b) CC

The average bond stress (τ) is defined as the axial load normalized by the contact area between the concrete jacket and steel pile and shown in equation 4.1.

$$\tau = \frac{F}{p\ L_e} \tag{4.1}$$

where *F* is the applied axial load at the free loaded end, and *p* is the perimeter of the H-pile cross-section in contact with the concrete jacket. Equation 4.1 assumes uniform bond stress distribution along the encasement length of the steel pile.

The calculations of relative slip between the H-pile and the concrete jacket at the loaded end ignore the axial deformation in the steel pile specimen, which can be justified given the short gauge length of the LVDT and the low stresses in the steel sections until the failure of the concrete jackets.

Three intercorrelated mechanisms control the general mechanics of stress transfer by the bond between steel elements embedded in concrete: (a) concrete chemical adhesion, (b) friction between the steel element and concrete, and (c) mechanical interlocking offered by the deformation of the interface surface roughness (Abdulazeez et al. 2019; du Béton 2000; Hadi 2008; Harajli 2009; Raynor et al. 2002). In this study, the surface of the H-pile was quite smooth; thus, mechanical interlocking was minimal, and only chemical adhesion and friction were considered.

4.5.1 Failure Modes

Figure 4.5 shows the failure modes of the tested specimens. In general, the splitting of the concrete jacket occurred along the encasement length. As shown in figure 4.4, the failure produced a drop in the bond resistance with an increase in the slip because of the propagation of the cracks at the smallest concrete jacket thickness.

In the case of the UHPC encased specimens, no sudden failure was observed at the peak load. The cracks were initiated at the flange or its side and extended towards the jacket's outer circumference. Because of the presence of steel fibers in the case of UHPC jackets, the number of cracks was smaller than that in the case of CC. Similarly, the propagation of cracks in the case of UHPC was much slower than that in the case of CC. In the case of the CC specimens, sudden splitting of concrete occurred with rapid propagation of the cracks, starting at the tips of the flanges and extended toward the concrete outer perimeter (fig. 4.5b).

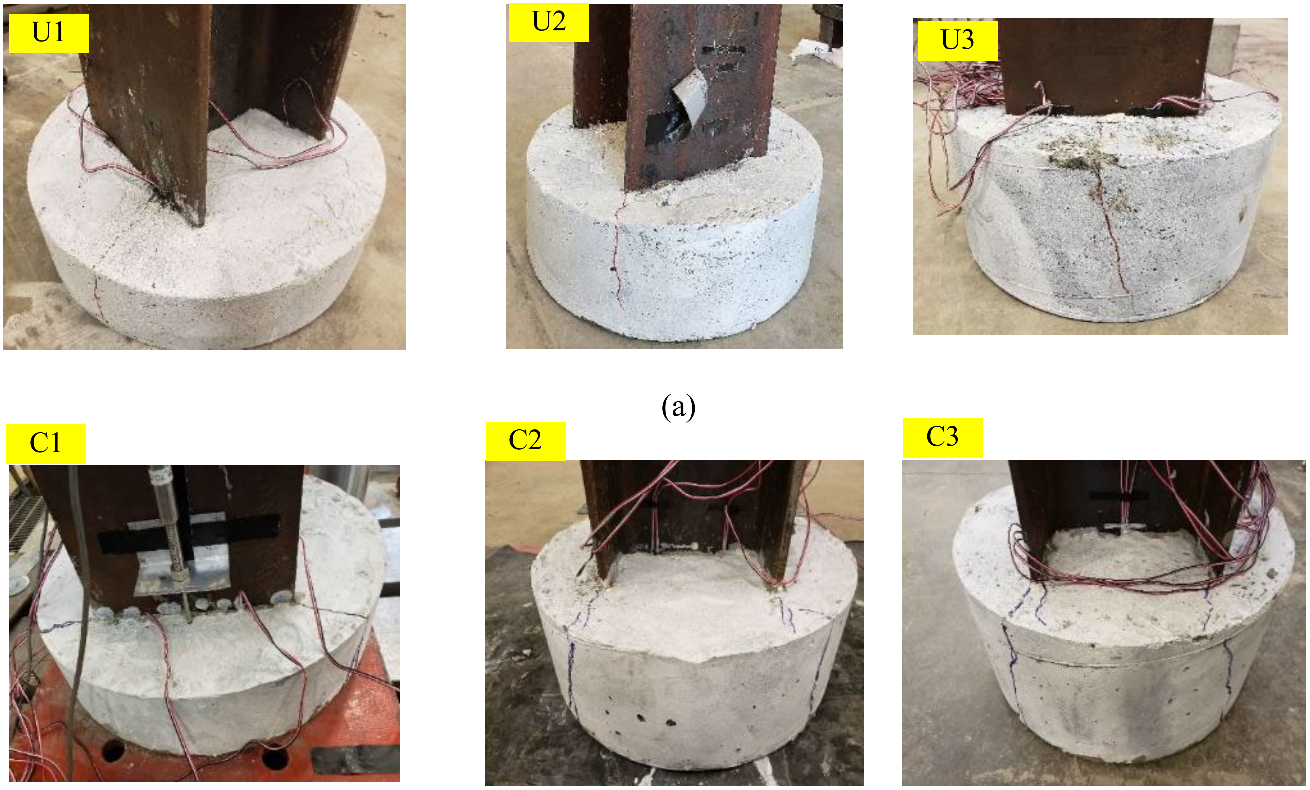

(a)

(b)

Figure 4.5 Modes of failure of the tested specimens (a) UHPC, and (b) CC

4.5.2 Effect of Encasement Length, Le

The results of the push-out test performed on the steel H-pile encased with different concrete jackets are summarized in table 4.4.

Table 4.4 Results of the Push-out Tests

Specimen ID	L_e (in.)	Peak Load (P_o) (kips)	Maximum Bond Stress (τ_o) (ksi)	Slip (δ_o)* (inch x 10^{-2})
U1	2.5	24.9	0.17	0.67
U2	5.0	59.3	0.20	1.56
U3	7.5	109.1	0.25	6.18
C1	2.5	5.37	0.037	2.61
C2	5.0	23.5	0.080	0.48
C3	7.5	37.6	0.085	0.32

** At the peak load*

Figure 4.6a shows the bond strength τ_o versus the encasement length L_e. Three different encasement lengths, of 2.5 in., 5 in., and 7.5 in. have been investigated in this study. In general, as L_e increased, the bond strength increased (fig 4.6a, table 4.4).

The specimens having UHPC jackets displayed τ_o ranging from 0.17 ksi to 0.25 ksi (table 4.4). This represented increments of 19% for L_e of 5 in., and 46% for L_e of 7.5 in., when compared to that of specimens having L_e of 2.5 in. For the design of UHPC concrete jackets for steel piles, a τ value of 0.2 ksi represents a reasonable assumption.

The specimens with CC jackets displayed a τ_o ranging from 0.037 ksi to 0.086 ksi (table 4.4). This represented increments of 119% for L_e 5 in., and 133% for L_e of 7.5 in., when compared to that of specimens having L_e of 2.5 in. For the design of CC concrete jackets for steel piles, a τ value of 0.08 ksi represents a reasonable assumption.

4.5.3 Effect of Different Concrete Jacket Types

Figure 4.6b shows the test specimens with the different concrete jackets grouped based on L_e. Expectedly, τ_o is higher in the case of UHPC compared to that of CC for each L_e. For specimens with 2.5 in. L_e, the UHPC jacket displayed 364% higher τ_o than that of the CC jacket. This increment is the highest among all specimens. For the specimens with L_e of 5 in. and 7.5 in., the UHPC jacket displayed 152% and 195% higher τ_o than that of the CC jacket, respectively.

It is noted that the AISC (2010) recommends a concrete/steel bond shear strength of 0.20 ksi for concrete-filled HSS having circular cross-sections. For the UHPC jackets with L_e of 5 in. and 7.5 in., the bond strength exceeded the AISC (2010) recommended value by 1% and 23%, respectively (figs. 4.6a and b). However, for UHPC with 2.5 in. L_e the bond strength failed to meet the AISC recommended value. A similar case was observed in the case of all CC specimens.

Figure 4.6c illustrates the encasement length L_e versus the bond strength (τ_o) of the tested specimens normalized by $\sqrt{f'_c}$ to eliminate the influence of the variation in the tensile strength of different types of concrete. As shown in the figure, the normalized bond strength $(\tau_o/\sqrt{f_c'})$ for the UHPC specimen was 44% to 165% higher than that of the CC specimens.

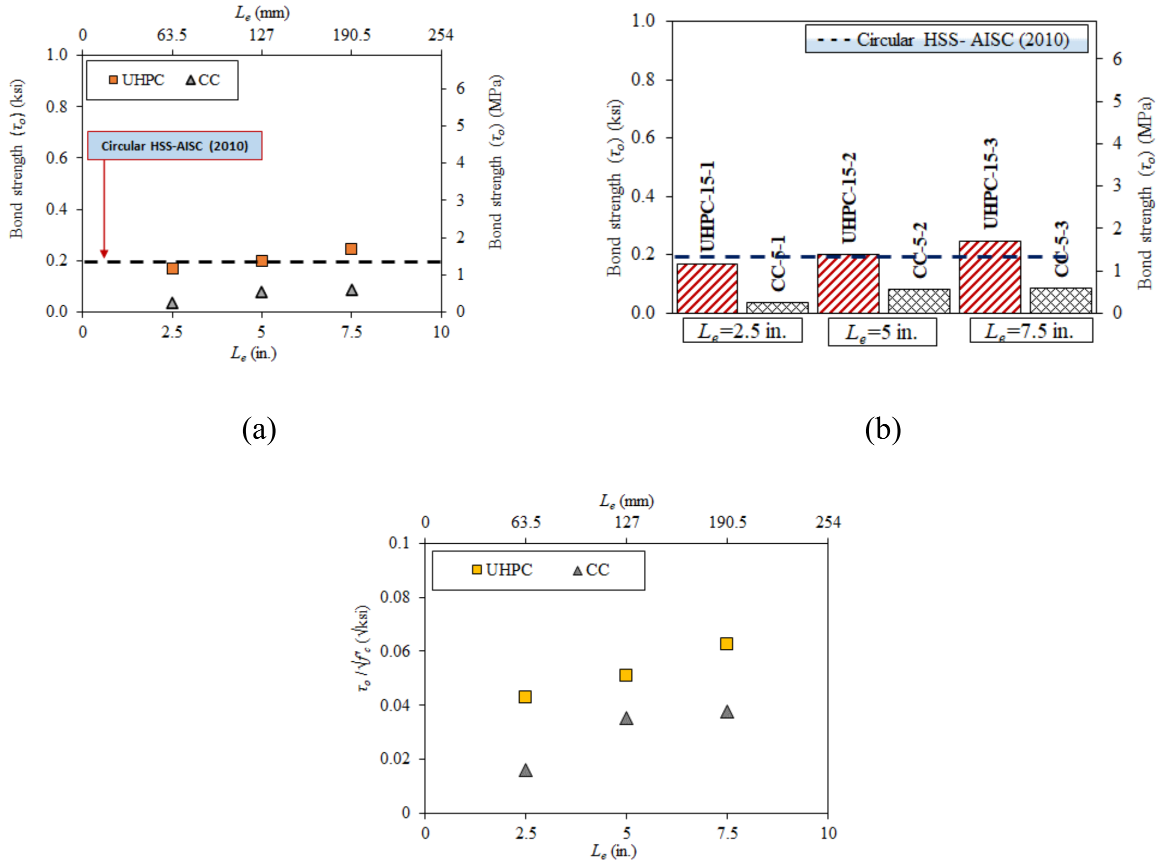

(a)

(b)

(c)

Figure 4.6 Bond strength, τ_o: (a) versus the encasement length L_e, (b) of the tested specimens, (c) normalized by $\sqrt{f'_c}$ versus L_e

4.5.4 Axial Strain Distribution

Figure 4.7 shows the axial strain distribution along the encasement length, L_e. The axial strains induced along the encasement length of each H-pile during testing were measured. The reported strains are the average strain measurements at a given section and load. The encasement length is measured from the loaded end of the H-pile. The strain distributions were shown for each 25% increment of peak axial load (P_o). Further, the solid line in figure 4.7 represents the axial strains at the onset of bond breaking. In general, the axial strain increased when increasing the applied load and decreased when increasing the distance from the loaded end. A significant strain gradient, found in the region near the loaded end, reflects the transmission of interfacial shear stress.

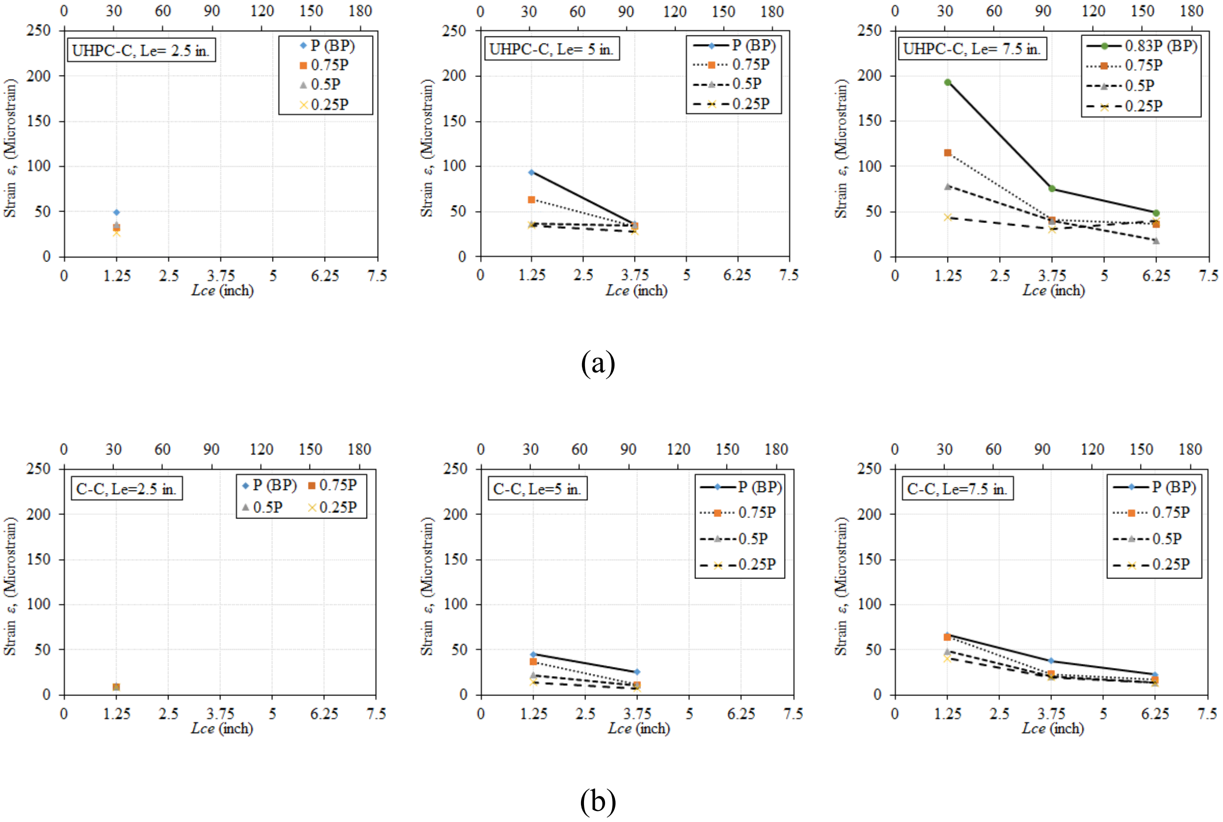

(a)

(b)

Figure 4.7 Axial strain distribution along the encased length at the different load percentages: (a) UHPC, and (b) CC

Chapter 5 Behavior of Steel Piles Repaired Using Ultra-High Performance Concrete Plates

This chapter presents the experimental results of two phases to develop an Ultra-High Performance Concrete (UHPC) repair methodology for corroded H-piles. During Phase I, push-out testing was conducted on eleven short H-piles encased in prefabricated UHPC plates attached to the H-piles using shear connectors. The push-out tests were used to assess the axial force that can be transferred through shear connectors. Considering different construction and handling factors, the dimensions of the prefabricated UHPC plates were selected to be as light and thin as possible such that they can be easily handled on a construction site. The maximum thickness of the UHPC plate was selected as 2.25 in. During Phase II, the optimized UHPC plates from Phase I were used to repair three full-scale corroded H-piles and then tested them under axial compression.

5.1 Experimental Program

The experimental program consisted of the following two phases.

5.1.1 UHPC-Phase I: Push-out Testing

A total of eleven HP10 x 42 steel H-piles subjected to push-out testing were investigated (table 5.1). The test parameters were the thickness of the UHPC plate (t_{UHPC}), the diameter of shear connectors (SC), and the number of layers of carbon fiber reinforced polymer (CFRP) grid. Each UHPC plate had a length of 12 in.. High strength bolts with diameters of 0.5 in., 0.75 in., and 1.0 in. were used as shear connectors (SCs). The UHPC plates were reinforced with one, two, or four layers of CFRP grid (fig. 5.1c and d).

The UHPC plates were attached to the H-piles using shear connectors (fig. 5.1) such that a 2.0 in. gap was left underneath the H-pile to accommodate the slip between the panels and the H-piles during the push-out testing (fig. 5.1a). The bolts were installed with a preset torque of 9.3

kips-ft using a torque wrench. An approximately 0.25 in. layer of hydro-stone was placed underneath the base of UHPC panels to ensure the full contact between the UHPC and the base plate during testing (fig. 5.1b).

The specimens in table 5.1 were labeled as follows: #t, indicating the thickness of the UHPC plate, #SC, indicating the diameter of the shear connectors in inches, which is followed by #CG, the number of CFRP grid layers. For example, specimen 0.75t-1/2SC-2CG was a steel pile repaired using 0.75 in. UHPC plates, 0.5 in. shear connectors, and 2 layers of CFRP grid.

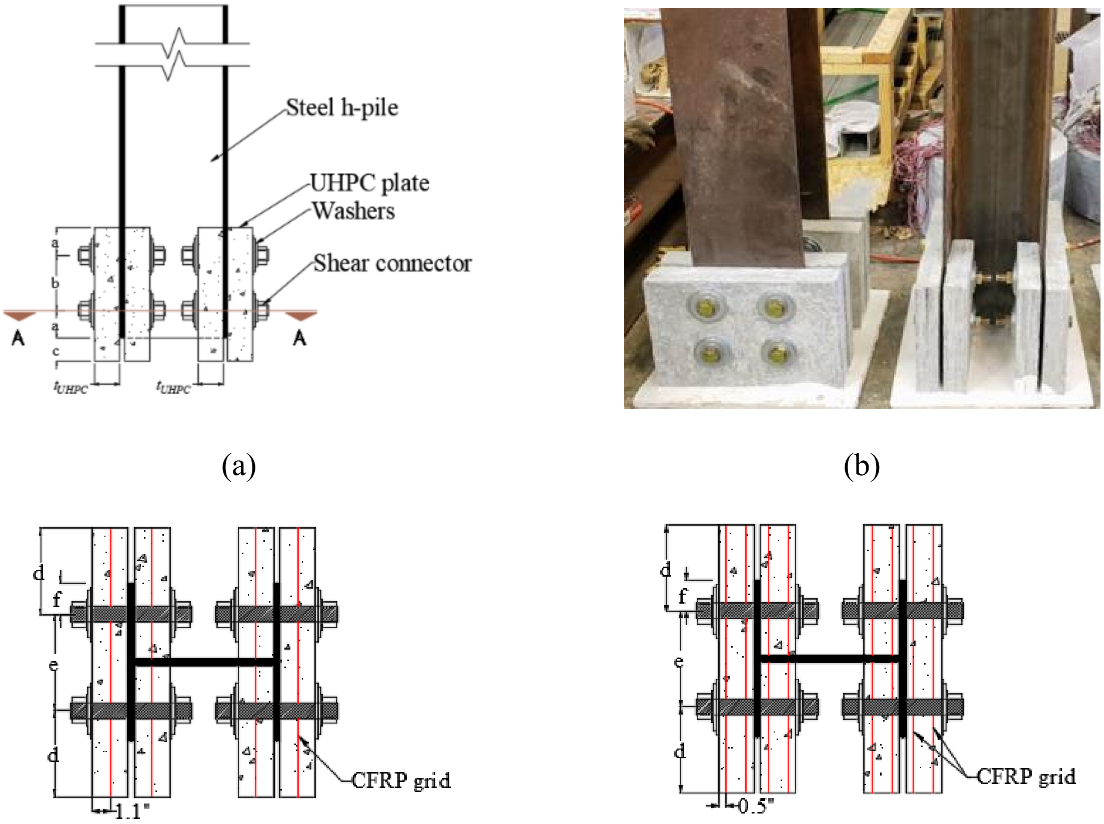

(a)

(b)

(c)

(d)

a = 2.5 in., b =5 in., c = 2 in., d = 5.5 in., e = 6 in., f = 2 in.

Figure 5.1 Test specimens of UHPC-Phase I: (a) layout, (b) specimens ready for testing, (c) section A-A with one layer of CFRP grid, and (d) section A-A with two layers of CFRP grid

5.1.2 UHPC-Phase II: Large-scale Repair System

A total of three 120 in. long large-scale corroded HP10 x 42 steel H-piles repaired with UHPC plates subjected to concentric axial compression testing were investigated (table 5.1). The corroded steel H-piles selected for Phase II are W70-F50-30%, W70-F00-30%, and W70V-F50-0%. These piles represent heavily corroded piles with local buckling and local yielding. They were previously tested during the assessment task and were reused in Phase II after straightening them. The H-piles were straightened using a hydraulic jack to restore their original alignment as much as possible.

Table 5.1 Test Program: UHPC-Phase I

Group	Specimen Name	t_{UHPC} (in.)	SC			No. CFRP Grid Layer(s)
			No.	Row	Dia. (in.)	
A	0.75t-1/2SC-1CG	0.75	8	2	0.5	1
	1.5t-1/2SC-1CG	1.5				1
	1/2SC-1CG	2.25				1
	1/2SC-2CG					2
B	3/4SC-1CG	2.25	8	2	0.75	1
	3/4SC-2CG					2
	3/4SC-4CG					4
C	0.75t-1SC-1CG	0.75	8	2	1	1
	1.5t-1SC-1CG	1.5				1
	1SC-1CG	2.25				1
	1SC-2CG					2

After straightening up the H-piles, any bumps on the flanges and the web obstructing the UHPC plates attachment were cut, and the required number of holes for the high-strength (HS) bolts were drilled using a magnetic drill. The UHPC plates were attached to the H-pile with HS bolts and heavy hex nuts with a preset torque of 9.3 kips-ft using a torque wrench as in UHPC-Phase I (fig. 5.3c). The details of the UHPC plates, i.e., UHPC plat thickness, bolt diameters, and

CFRP grid layers, were determined based on the results of the UHPC-Phase I and are shown in table 5.2.

Table 5.2 Test Program: UHPC-Phase II

Specimen Designation	Specimen Name	UHPC		Shear Connectors (SC)			CFRP Grid Layers
		Length (in.)	t_{UHPC} (in.)	No.	Row	Dia. (in.)	
R1	UHPC-0.75SC-2CG	32	2.25	16	4	0.75	2
R2	UHPC-1SC-1CG					1	1
R3	UHPC-1SC-2CG					1	2

5.2 Material Properties

5.2.1 H-pile

The mechanical properties of a steel H-pile for this chapter are the same as specified in table 3.3 of Chapter 3.

5.2.2 Ultra-high-performance Concrete (UHPC)

The UHPC was developed as described in Section 4.2.2 of Chapter 4.

The average compressive strength, f'_c, and tensile strength, f'_t, of the UHPC on the day of testing were 19.2 ksi and 2.6 ksi, respectively.

5.2.3 Shear Connector (SC)

High-strength bolts of grade ASTM A490 with a minimum tensile strength of 150 ksi with diameters of 0.5 in., 0.75 in., or 1.0 in. and heavy hex nuts were used to attach the UHPC plates to the H-piles. Steel washers with outer diameter/thickness of 2 in./ 0.134 in., 3.0 in./0.156 in., and 3.5 in./0.140 in. were used between the UHPC and heavy hex nuts as well as bolt head and UHPC to reduce the stress concentration.

5.2.4 Carbon Fiber Reinforced Polymer (CFRP) Grid

One, two, or four layers of carbon fiber reinforced polymer (CFRP) grids were embedded in the UHPC plates. The nominal spacing of each CFRP grid in the transverse and longitudinal direction was 1.6 in. and 1.8 in., respectively. Table 5.3 shows the mechanical properties of the individual strands of the CFRP grids provided by the manufacturer.

Table 5.3 Mechanical Properties of an Individual Strand of CFRP Grid

Direction	Tensile Strength Per Unit Width, (lbs/ft)	Tensile Modulus of Elasticity, (ksi)	Elongation at Break, %
Transverse	5,480	34,000	0.76
Longitudinal	5,530	34,000	0.76

5.3 Preparation of Test Specimens

The surface of each H-pile was cleaned using power hand tools to remove dirt, dust, and rust as per the Society for Protective Coatings Standards (SSPC-SP 2015). The formworks with CFRP grids were prepared, as shown in figure 5.2a. The CFRP grid was cut to the required dimensions, and the ends were embedded on the sides of the formwork. Concrete cover thicknesses of 1.5 in. and 0.5 in. were used when there was one or two layers of CFRP grid. In the case of four layers, two layers of CFRP grids were bundled together and a concrete cover thickness of 0.5 in. was used.

The fresh UHPC mix was placed in the formworks (fig. 5.2b) without using any mechanical vibrators or tamping rods. Numerous 2.0 in. standard cubes and 3.0 x 6.0 in. cylinders were also cast. The specimens and the formworks, including cubes and cylinders, were then covered with plastic sheets to prevent moisture loss. They were demolded after 24 hours of placing the UHPC.

After demolding, the UHPC plates (fig. 5.2c), cylinders, and cubes, were cured inside the steam chamber at a maximum temperature of 158º F for 24 hours. They were then cured in a moisture room with a relative humidity of 95 ± 5% until the day of testing. Once the target compressive strength of the UHPC was achieved, the curing was stopped.

(a) (b) (c)

Figure 5.2 Preparation of UHPC plates: (a) formworks, and (b) casting of UHPC, and (c)UHPC plates ready to be attached to H-piles

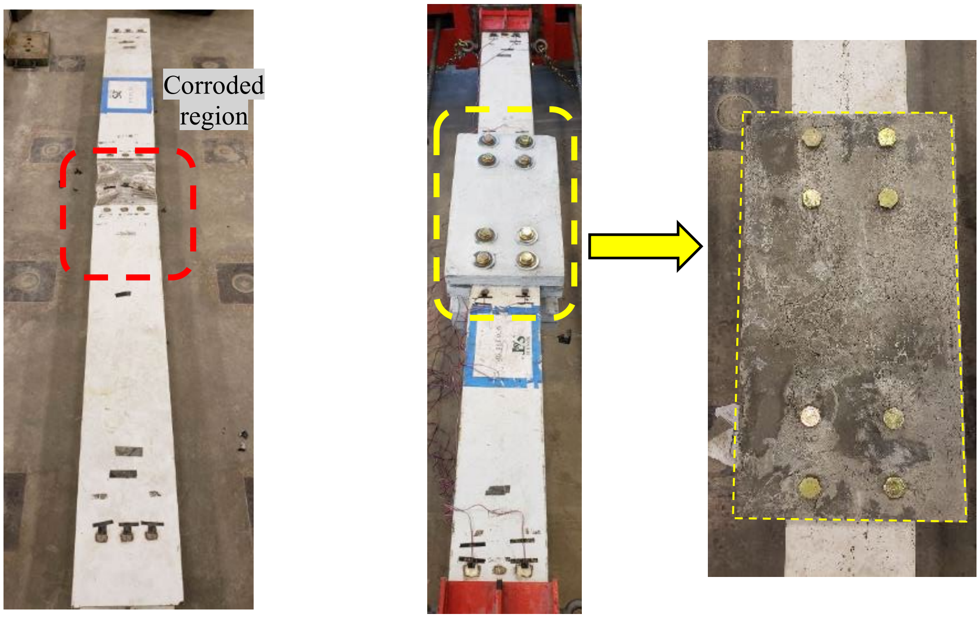

(a) (b) (c)

Figure 5.3 Repair of H-piles using UHPC plates during UHPC-phase II: (a) straightened H-pile before repair, (b) repair using UHPC plates, and (c) enlarged repaired pile segment

5.4 Test Instrumentation and Setup

5.4.1 Phase I Testing

All specimens from Group A and two specimens from group C, 0.75t-1SC-1CG and 1.5t-1SC-1CG (table 5.2), were tested using a 550 kips MTS universal testing machine (fig. 5.4a) while the remaining specimens were tested using the 1000 kips self-sustained testing frame (SSTF) (fig. 5.4b and c) that was described in Chapter 3. This difference in testing setups depended on the anticipated axial capacity of the tested specimens.

In SSTF, two string potentiometers were attached to the movable beam at one end and the rigid beam at the other end along the length of a test specimen.

5.4.2 Phase II Testing

The H-pile with the UHPC repair system was subjected to axial compression using the SSTF described in Chapter 3 (fig. 5.4d). Twenty-eight strain gauges were attached to the web and flanges of each H-pile specimen to measure the axial strains. As in the UHPC-Phase I, two string-potentiometers were attached between the movable and rigid beams along the length of each specimen. Furthermore, five string-potentiometers were installed to measure the lateral displacements of each H-pile along its length. Three string pots were also installed to measure the vertical displacement of each pile as described in Chapter 3.

5.5 Results and Discussion

5.5.1 UHPC-phase I: Push-out Testing

5.5.1.1 Modes of Failure and Axial Strength

Figure 5.5 displayed the specimens after testing. Figure 5.6 shows the axial force vs. displacement curve. The push-out test results and the description of the failure modes for all specimens are tabulated in table 5.4. The failure modes of the tested specimens can be categorized in: (i) shear-off of the shear connector (SC), and (ii) splitting and crushing failure of the UHPC. Figure 5.5a shows the typical failure modes of specimens with a ½ in. bolted shear connector, dominated by bolt shear-off at the interface. Specimens such as 1.5t-1/2SC-1CG, 2.25t-1/2SC-1CG, and 2.25t-1/2SC-2CG showed similar axial force vs. displacement behavior (fig. 5.6b-d). At the early loading stage, almost no slipping was observed between the UHPC plates and H-piles, with the shear connection having a very high stiffness due to the pretension of the bolted shear connectors.

As the mechanical friction at the interface between the SC and UHPC plates was overcome at about 8 kips, slip occurred and the bolts bore against the surface of the hole in the

UHPC plate. With continuous loading, specimens 1.5t-1/2SC-1CG, 2.25t-1/2SC-1CG, and 2.25t-1/2SC-2CG reached their peak axial loads ($P_{\max}$) of 291 kips, 287 kips, and 295 kips, corresponding to about 45- 47% of the squash load (P_o) of the H-piles, at a displacement of 0.32 in., 0.25 in., and 0.29 in., respectively.

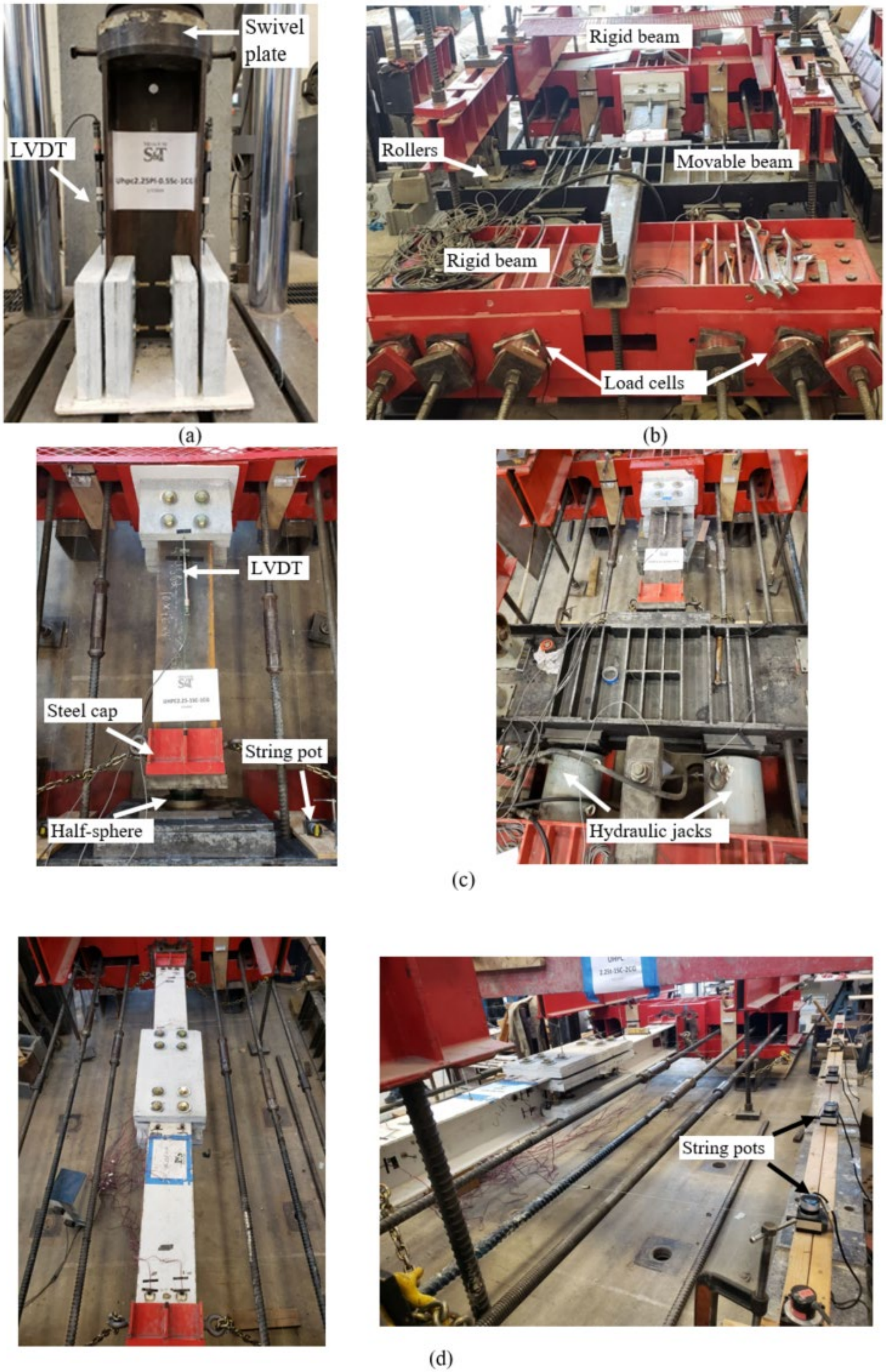

Figure 5.4 Test setup with instrumentation: (a)-(c) UHPC-phase I, and (d) UHPC-phase II

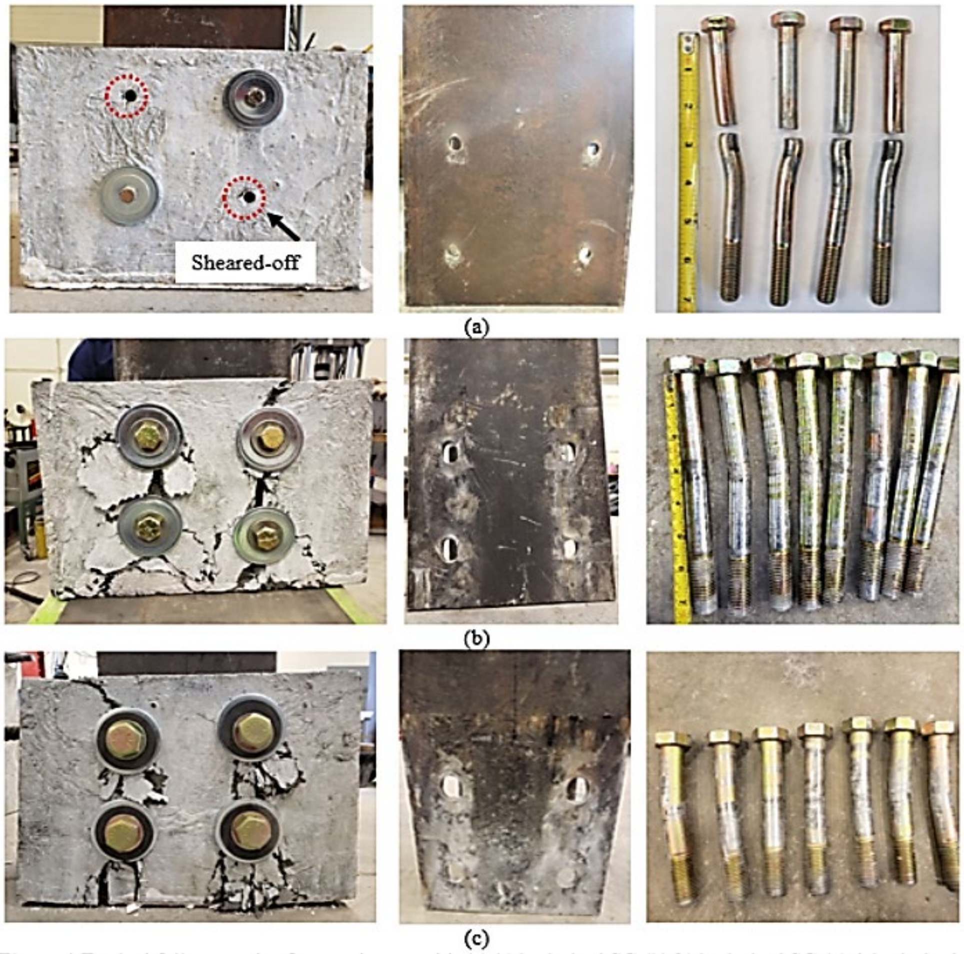

Figure 5.5 Typical failure modes for specimens with (a) ½ in., (b) ¾ in., and (c) 1 in. diameter SC

This was followed by the shearing-off of a top bolt from each flange (fig. 5.5a) and the drop of about 17%, 15%, and 21% of the $P_{\max}$ in the case of 1.5t-1/2SC-1CG, 2.25t-1/2SC-1CG, and 2.25t-1/2SC-2CG, respectively. Further, shearing-off of a bottom bolt from each flange occurred, dropping the axial load to about 42%, 51%, and 45% of the $P_{\max}$ in the case of 1.5t-1/2SC-1CG, 2.25t-1/2SC-1CG, and 2.25t-1/2SC-2CG, respectively. With the shearing-off of each bolt, the stepwise drop in the axial load was observed, as shown in fig. 5.6b-d, demonstrating a brittle mode of failure. A loud noise was heard on each shearing-off failure. However, no damage was observed in the UHPC plates.

Table 5.4 Push-out Test Results of UHPC Encased H-pile

Group	Specimen Name	Peak Load (P_{max}), (kips)	Displacement (δ_{max}*), (in.)	P_{max}/P_o**	Failure Mode
A	0.75t-1/2SC-1CG	219	0.41	0.35	UHPC splitting and crushing
	1.5t-1/2SC-1CG	291	0.32	0.46	SC shear-off
	2.25t-1/2SC-1CG	287	0.25	0.456	
	2.25t-1/2SC-2CG	295	0.29	0.468	
B	2.25t-3/4SC-1CG	502	0.486	0.797	UHPC splitting & crushing
	2.25t-3/4SC-2CG	536	0.52	0.851	
	2.25t-3/4SC-4CG	506	0.53	0.803	
C	0.75t-1SC-1CG	279	0.15	0.44	
	1.5t-1SC-1CG	542	0.31	0.86	
	2.25t-1SC-1CG	615	0.35	0.976	
	2.25t-1SC-2CG	605	0.39	0.960	

* at peak load

** P_o- squash axial load of un-corroded H-pile = 630 kips

By using equation 5.1 (ACI-318 2014), the nominal shearing off the strength of the bolt (V_{sa}) was calculated as 282 kips, representing on average 97% of the $P_{\max}$ for specimens 1.5t-1/2SC-1CG, 2.25t-1/2SC-1CG, and 2.25t-1/2SC-2CG.

$$V_{sa} = 0.6A_{se}f_{uta} \tag{5.1}$$

$$A_{se} = \frac{\pi}{4}(d_{sa})^2 \tag{5.2}$$

where A_{se} = effective cross-sectional area of SC, with shear plane acting through the shank (in^2), f_{uta} = specified tensile strength of the SC (ksi), and d_{sa} = diameter of the SC (in.).

Figure 5.5b shows the typical failure modes of specimens 2.25t-3/4SC-1CG, 2.25t-3/4SC-2CG, and 2.25t-3/4SC-4CG, all with ¾ in. diameter shear connectors. The failure mode for those specimens was UHPC crushing and splitting as well as yielding of the SC. At early loading stages, no slippage was observed in the specimens, displaying high shear stiffness because of the mechanical friction along the steel-UHPC interface, caused by the pretension of the shear connectors. As the load increased to about 9 kips, the friction at the interface was overcome, slip occurred, and the SC began to bear against the UHPC plate. With a further increase in the applied load, cracks were observed on the UHPC underneath the top bolts. In the case of specimens 2.25t-3/4SC-1CG and 2.25t-3/4SC-2CG, the initial cracks were observed at 90% and 93% of P_{max}, whereas in the case of specimen 2.25t-3/4SC-4CG, the initial crack was observed at 64% of P_{max}. Specimens 2.25t-3/4SC-1CG, 2.25t-3/4SC-2CG, and 2.25t-3/4SC-4CG reached $P_{\max}$ of 502 kips, 536 kips, and 506 kips, corresponding to 79.7%, 85%, and 80.3% of the squash load of the piles, P_o, at a displacement of 0.486 in., 0.52 in., and 0.53 in., respectively.

With further loading, the initial cracks were extended, leading to a complete split of the UHPC plates through the locations of the SCs, as shown in figure 5.5b.

Figure 5.5c shows the typical failure modes of specimens with 1in. diameter shear connectors. The failure mode for these specimens was similar to that of specimens having ¾ in. SCs, that is UHPC splitting and crushing with yielding of the SCs. Up to the average load of about 12.5 kips. Slippage at the UHPC-steel interface was not observed because of the mechanical friction at the interface. Once the friction was overcome, slip occurred, causing the bolts to bear against the surfaces of the holes in the UHPC plates. As the load increased to about 90-93% of P_{max}, cracks developed underneath the SCs at the lower end of the UHPC plates. Specimens 2.25t-1SC-1CG and 1SC-2CG reached P_{max} of 615 kips and 605 kips, corresponding to 98% and 96% of P_o, at a displacement of 0.35 in., and 0.39 in., respectively. With further loading, the cracks extended, triggering a complete split of the UHPC plates along with the SC, as shown in figure 5.5c.

5.5.1.2 Effect of UHPC Plate Thickness, Bolt Diameter, and CFRP Grids

Expectedly, the axial load increased with an increase in the diameter of the shear connector (table 5.4 and fig. 5.7a). In the case of specimens with a single layer of CFRP grid, increasing the SC diameter from ½ in. to ¾ in. and 1 in., corresponding to increments of 125% and 300% in the cross-sectional area, led to a 75% and 114% increase in P_{max}, respectively. Similarly, in the case of specimens with a double-layer of CFRP grid, when the diameter of the SC was increased from ½ in. to ¾ in. and 1 in., P_{max} increased by 80% and 105%, respectively. Furthermore, changing the diameter of the SC from ½ in. to ¾ in. and 1 in. changed the mode of failure from bolt shear off in the case of specimens 1/2SC-1CG and 1/2SC-2CG to UHPC splitting and crushing in the remaining specimens. Furthermore, it changed the axial load vs. displacement behavior from brittle to ductile behavior.

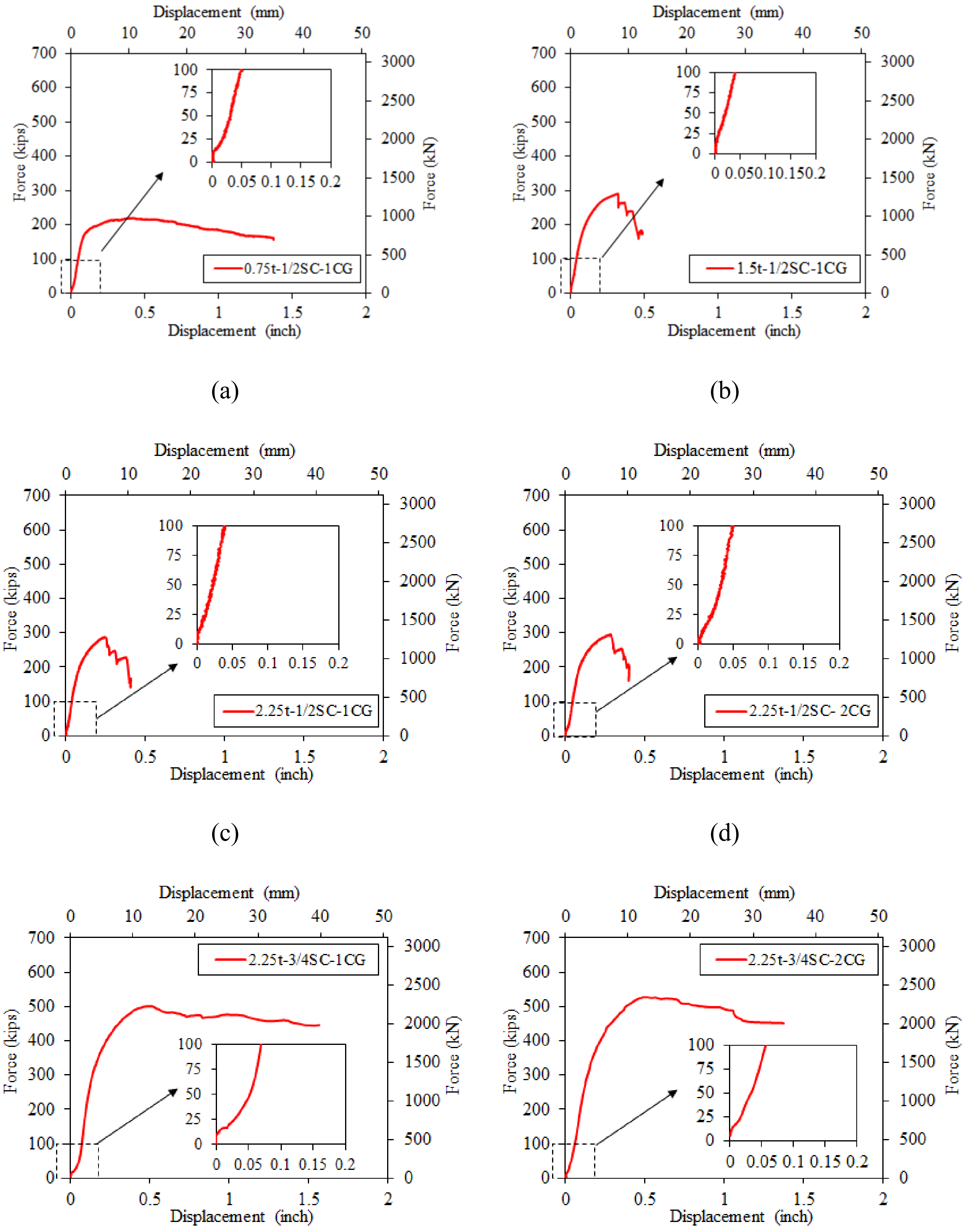

(a)

(b)

(c)

(d)

(e)

(f)

Figure 5.6 Force vs displacement curves of the specimens in the UHPC-phase I testing

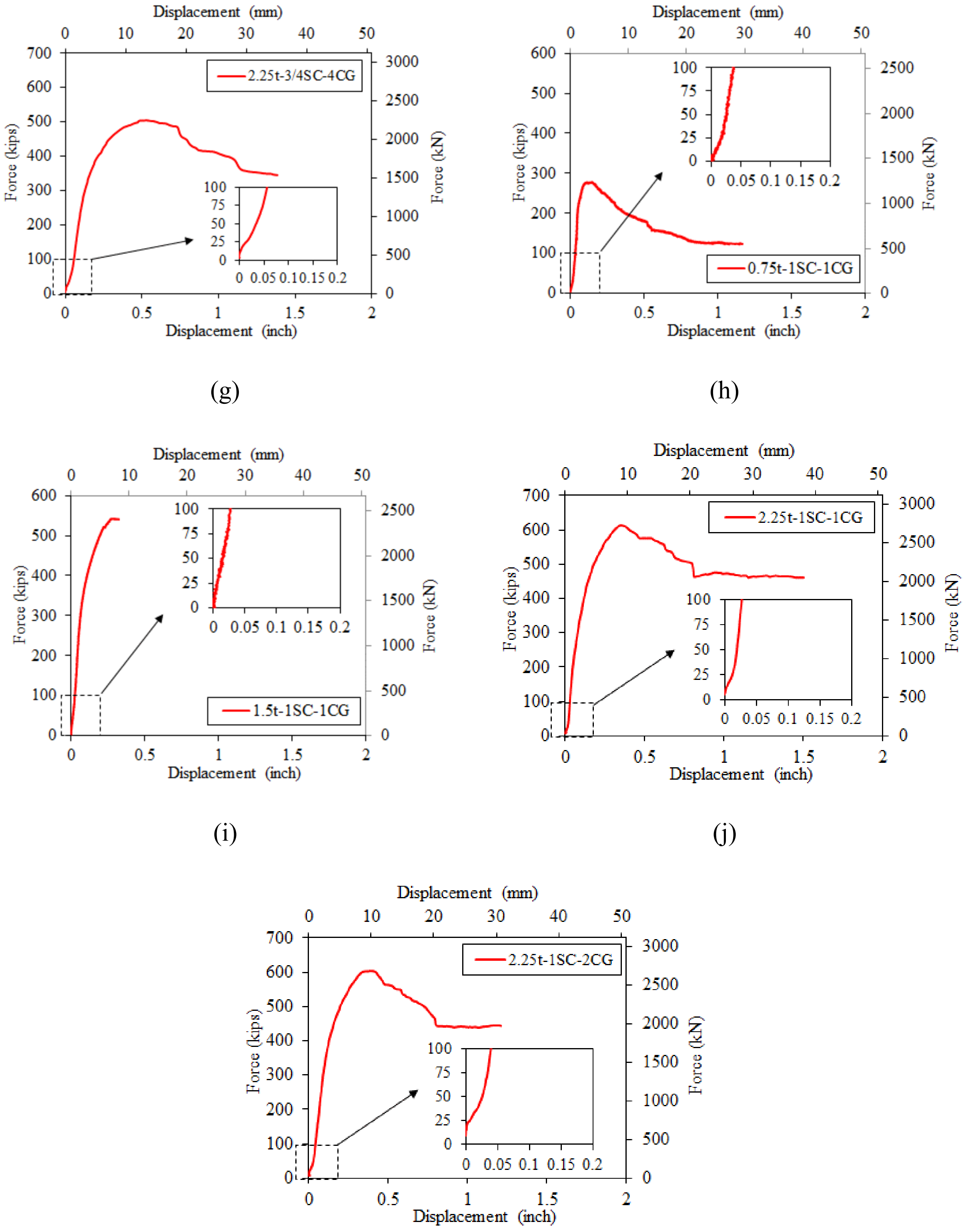

(g)

(h)

(i)

(j)

(k)

Figure 5.6 cont. Force vs displacement curves of the specimens in the UHPC-phase I testing

Figure 5.7b shows the effect of CFRP grid layers on the axial load. The axial load of the specimens does not correlate well with the CFRP grid layers. When the CFRP grid layer was increased from single to double layers, $P_{\max}$ increased by 3% and 6% for the specimens with ½ in. and ¾ in. diameter SC, respectively. However, for the specimens with double layers of CFRP grid with 1 in. SC displayed a 1.6% lower $P_{\max}$ than that of the specimens with single layers of the CFRP grid. Furthermore, for the specimens with ¾ in. SC, the value of $P_{\max}$ decreased from 536 kips to 506 kips when the CFRP layer increased from double-layer to four layers. The change in CFRP grid layers has little or no effect on the behavior of the axial load versus displacement.

Figure 5.7c shows the effect of the thickness of the UHPC plate on the axial load. In the case of specimens having a single layer of CFRP grid with 0.5 in. diameter bolts, increasing the thickness from 0.75 in. to 1.5 in. and 2.25 in., corresponds to increments of 100% and 200%, and displays a 33% and 31% increase in $P_{\max}$, respectively. Similarly, in the case of specimens having a single layer of CFRP grid with 1 in. diameter bolts, when the thickness was increased from 0.75 in. to 1.5 in. and 2.25 in., $P_{\max}$ increased by 148% and 180%, respectively.

Figure 5.7d shows the ratio of peak axial load ($P_{\max}$) of the tested specimens to the squash load (P_o) of an un-corroded H-pile. A ratio equal to one indicates that the specimen is able to transfer 100% of the axial load through the shear connector and friction between the UHPC and H-pile during the push-out testing. As shown in the figure, specimens with 1 in. diameter SC were capable of transferring 96% of P_o for specimen 2.25t-1SC-2CG and 98% for specimen 2.25t-1SC-1CG.

The axial force applied to the H-pile during the push-out testing is transferred through the SC in the form of shear force at the connection between steel and concrete. Current design codes such as AISC 2017, AASHTO LRFD 2012, and Eurocode-4 (EC-4) provide equations, based on the failure mode, to compute the shear strength of an SC embedded in the normal strength concrete. Eqation 5.3 is provided by AISC 2017 and AASHTO LRFD 2012 for SC failure strength.

$$V_{RS} = A_{se} f_u \tag{5.3}$$

where V_{RS} = ultimate shear connector resistance for shear connector failure in kip; A_{se} = cross-sectional area of a shear connector in in^2; and f_u = specified minimum tensile strength of a shear connector in ksi.

The Eurocode-4 (EC-4) suggests a reduction factor of 0.8 to equation 4.3 to compute the V_{RS} (eqn. 5.4):

$$V_{RS} = 0.8 A_{se} f_u \tag{5.4}$$

For concrete failure, AISC 2017 and AASHTO LRFD 2012 recommend the same equation to determine the ultimate shear connector resistance (V_{Rc}) (eqn. 5.5):

$$V_{Rc} = 0.5 A_{se} \sqrt{f'_c E_c} \tag{5.5}$$

where V_{Rc} = ultimate shear connector resistance for concrete failure in kip; f'_c = specified compressive strength of concrete in ksi; and E_c = modulus of elasticity of concrete in ksi.

The ultimate shear connector resistance for concrete failure provided by EC-4 2004 is given in equation 5.6.

$$V_{Rc} = 0.29\alpha d^2\sqrt{f'_c E_c} \qquad (5.6)$$

where α is the factor considering the height-to-diameter ratio of the SC, $\alpha = 0.2(h/d + 1) \leq 1$, and h and d are the height and diameter of the SC, respectively.

Both equations 5.3 and 5.4 were over-estimated the strength of the investigated specimens, with equation 5.4 being more accurate (table 5.5). A ratio of experimental to predicted value ranged from 32% to 63% and 40% to 78% using equations 5.3 and 5.4, respectively. Furthermore, the ultimate shear resistance for concrete failure (V_{Rc}) provided by equation4.5 was over predicted with the ratio of experimental to predicted value ranging from 13% to 53% compared to the experimental results. Equation 5.6, however, was found to have a better correlation with the experimental results with predictions ranging from 35% to 143% of the experimental results.

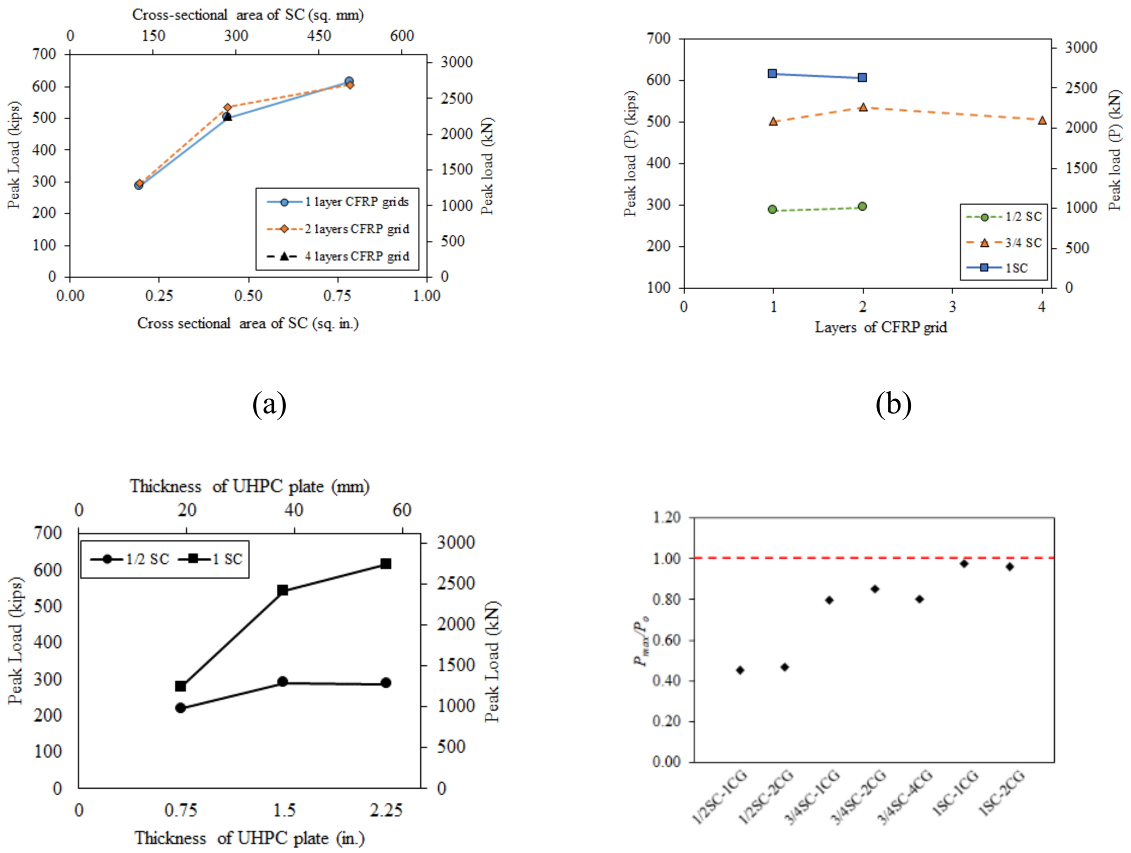

(a) (b)

(c) (d)

Figure 5.7 Parameters affecting P_{max} (a) effect of the cross-sectional area of shear connector (SC), (b) effect of number of layers of CFRP grid, (c) effect of thickness of UHPC plate on peak load (P), and (d) ratio of P_{max} to the nominal squash load of H-pile

5.5.2 UHPC-Phase II: Large-scale Repair System

5.5.2.1 Mode of Failure and the Axial Strength

Figure 5.8 shows the large-scale repaired H-pile before and after the axial test. Figure 5.9 illustrates the axial force versus axial shortening for the repaired H-piles. The axial shortening was obtained from the two SPs placed between the moveable beam at one end of the H-pile and the fixed beam at the other end of the H-pile. Table 5.6 shows summaries of the peak loads and axial shortenings at peak loads. The failure modes of the tested specimens were very similar; global buckling occurred in all H-piles, followed by splitting of the UHPC plates.

Table 5.5 Comparison of Predicted and Experimental Results

Specimen Name	Peak Load (P_{max}), (kips)	V_{RS} (SC failure)				V_{Rc} (concrete failure)			
		AISC, AASHTO (Eqn. 4.3) (kips)	P_{max}/V_{RS}	EC-4 (Eqn. 4.4) (kips)	P_{max}/V_{RS}	AISC, AASHTO (Eqn. 4.5) (kips)	P_{max}/V_{RC}	EC-4 (Eqn. 4.6) (kips)	P_{max}/V_{RC}
C1	219	471	0.46	377	0.58	546	0.40	202	1.09
C2	291		0.62		0.77	551	0.53	203	1.43
C3	287		0.61		0.76	555	0.52	205	1.40
C4	295		0.63		0.78	557	0.53	206	1.43
C5	502	1060	0.47	848	0.59	1254	0.40	463	1.08
C6	536		0.51		0.63	1249	0.43	461	1.16
C7	506		0.48		0.60	1249	0.41	461	1.10
C8	279	1885	0.15	1508	0.19	2186	0.13	807	0.35
C9	542		0.29		0.36	2203	0.25	813	0.67
C10	615		0.33		0.41	2220	0.28	820	0.75
C11	605		0.32		0.40	2246	0.27	829	0.73

Table 5.6 Summary Results of Tested Repaired H-piles During UHPC-phase II

S.N.	Specimen Name	Un-repaired Original Strength (kips)	Peak Load (kips)	Axial Shortening (in.)	% Increasing Strength
R1	UHPC-0.75SC- 2CG	265	481	-0.92	182
R2	UHPC-1SC-1CG	235	430	-0.67	183
R3	UHPC-1SC-2CG	199	445	-0.66	224

As shown in figure 5.9a, the peak load for specimen UHPC-0.75SC- 2CG was 481 kips, which showed an increase in the capacity of the H-pile by 82% compared to the corroded pile before repair using UHPC. A failure occurred due to global buckling about the x-axis, similar to the global buckling that occurred in the corroded pile before repair. Buckling led to tensile cracking and rupture of the top UHPC plate (fig. 5.8a). Similarly, for specimen UHPC-1SC-1CG, the capacity of the H-piles increased by 83% compared to the original corroded pile with the peak load reaching 430 kips (fig. 5.9b), and failure due to global buckling about the x-axis which triggered splitting cracking on the UHPC plates (fig. 5.8b).

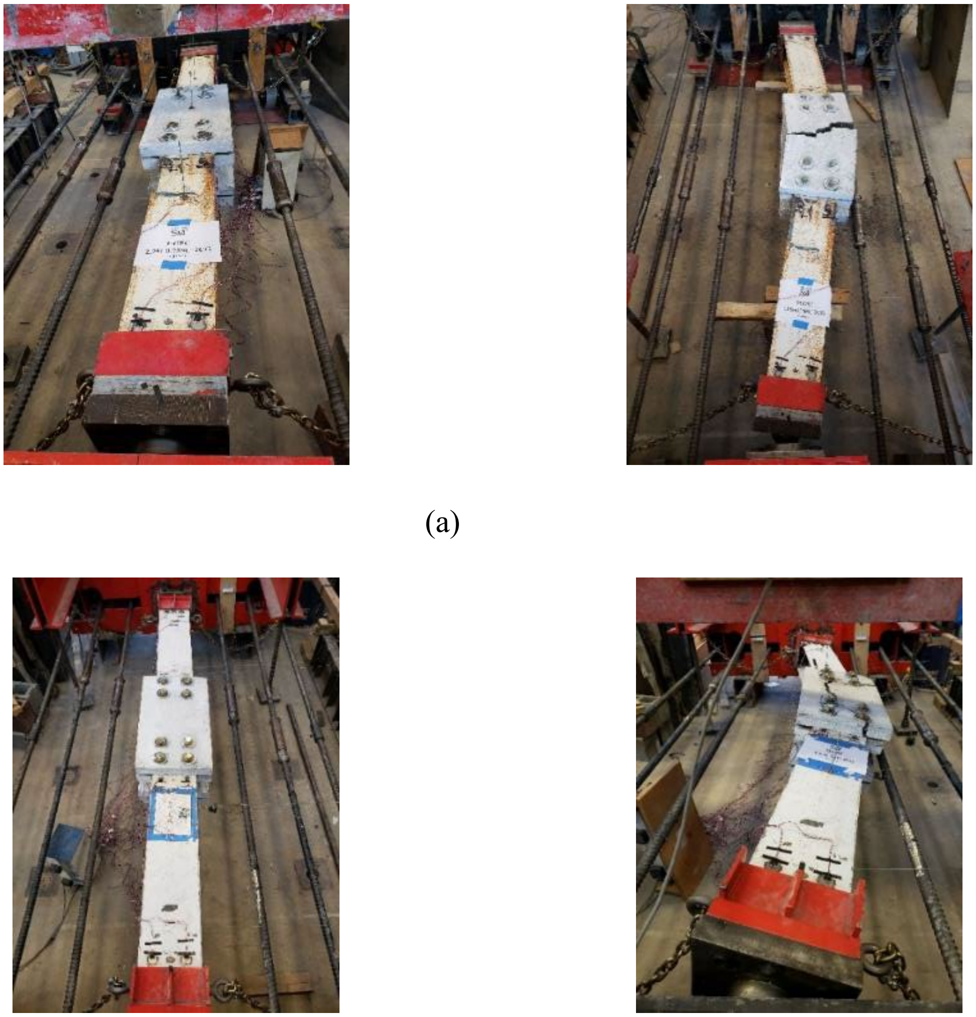

(a)

(b)

Figure 5.8 Repaired H-piles before and after the testing: (a) UHPC-0.75SC-2CG, (b) UHPC-1SC-1CG, and (c) UHPC-1SC-2CG

Furthermore, specimen UHPC-1SC-2CG displayed the highest increment of 124% in the axial capacity compared to the reference corroded pile reaching a peak load of 445 kips (fig. 5.9c). The failure mode was similar, however, to that which occurred during testing specimen UHPC-1SC-1CG (fig. 5.8c).

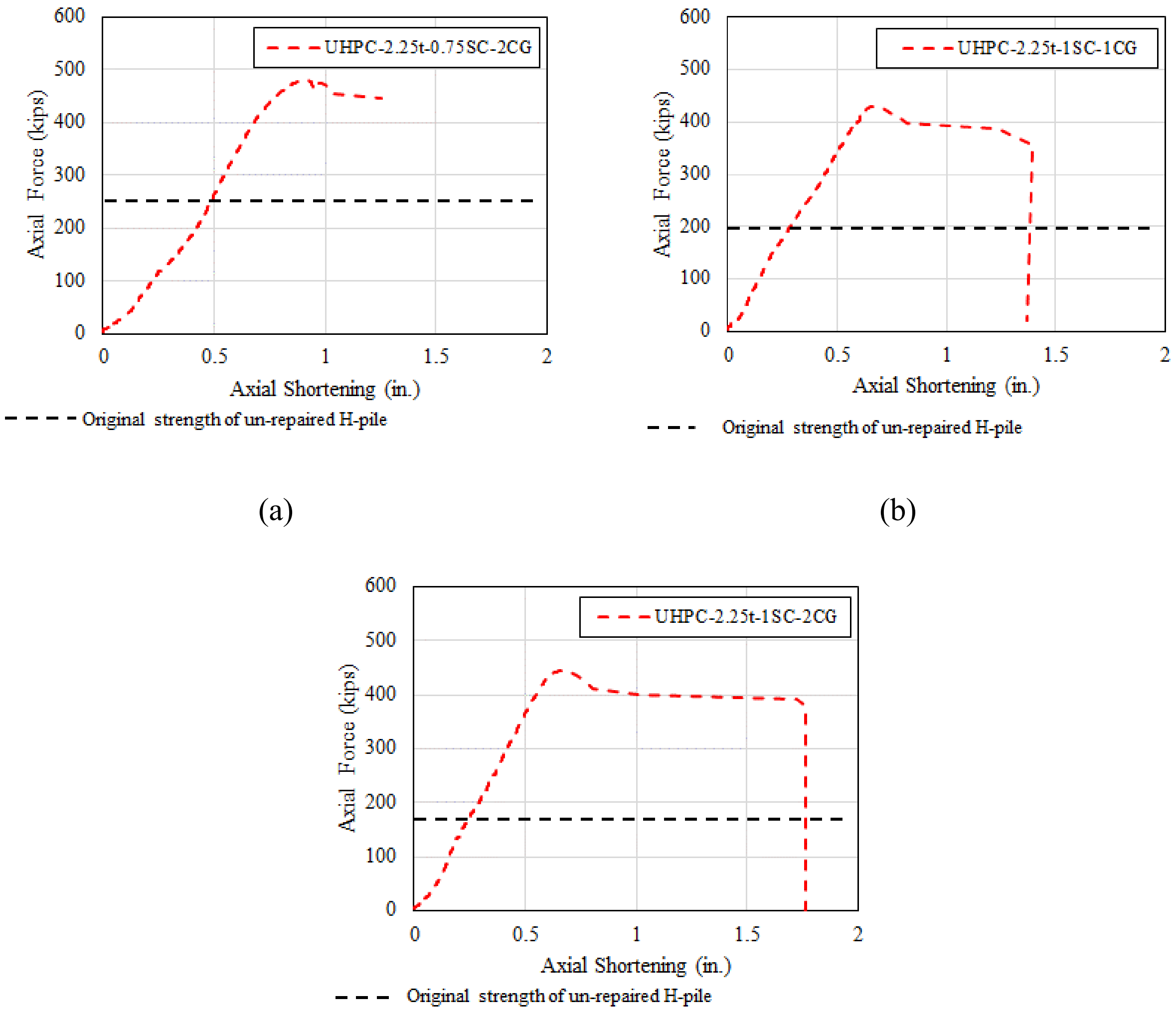

(a)

(b)

(c)

Figure 5.9 Axial force versus axial shortening of the repaired H-piles: (a) UHPC-0.75SC-2CG, (b) UHPC-1SC-1CG, and (c) UHPC-1SC-2CG

Chapter 6 Summary and Conclusions

This comprehensive report includes five chapters addressing the issue of assessment and repair of corroded steel H-piles. Two different repair options were investigated. This included using concrete-filled pultruded carbon fiber reinforced polymer tubes (CFPTs) and ultra-high-performance concrete (UHPC) plates. For each method, the repair procedure and design were optimized through experimental testing. Once the repair options were optimized, nine piles were repaired using different options. Furthermore, the durability of concrete encased in fiber-reinforced polymer tubes was determined. The experimental and analytical work presented in this report led to the following conclusions:

1. The failure mode of the CFPT specimens under the push-out testing was mainly splitting failure going through the concrete and FRP tubes along with the shear connectors.
2. Global buckling dominated the mode of failure of the CFPTs repaired full-scale corroded H-piles. Increasing the number of shear connectors (SCs) used to attach the FRP tubes to the repaired pile increased the repaired piles' strength.
3. The UHPC plates with 1 in. diameter shear connectors could transfer 96% to 98% of the H-piles' squash load. Furthermore, the proposed system is easy and fast to install. The plates are also relatively lightweight compared to conventional concrete or steel plates.
4. The load that can be transferred using UHPC plates did not depend on the number of CFRP grid layers. Increasing the number of CFRP grid layers from one to two layers increased the strength by 3% and 6% for the specimens with ½ in. and ¾ in. diameter of the shear connector, respectively. However, the specimens with double layers of CFRP grid with 1 in. shear connectors displayed a 1.6% lower strength than that of specimens with a single layer of the CFRP grid.

5. Changing the shear connector diameter used to attach the UHPC plates to the steel H-piles from ½ in. to 1 in. changed the mode of failure from bolts shear off to UHPC splitting and crushing.
6. Using the ACI 318 (ACI-318 2014) well predicted the shear connectors' shearing off strengths and the predicted strengths ranged from 98% to 96% of the measured strengths.

References

Abdulazeez, M., Sherstha, B., and ElGawady, M. "Retrofit of Corroded Steel H-Piles Using Concrete Encased in CFRP." *Proc., 10th New York City Bridge Conference, New York City, NY, USA*.

Abdulazeez, M., Sherstha, B., Gomaa, E., Ramadan, A., and ElGawady, M. M. (2019). "Bond Behavior of Steel H-Pile Bridge Columns Encased in Concrete Jackets." *Transportation Research Board, Washington, DC*.

Abdulazeez, M. M., Ramadan, A., Sherstha, B., Gheni, A., Gomaa, E., Darwish, Y., and ElGawady, M. (2019). "Behavior and Repair of Corroded Steel H-Piles Phase I (Axial Behavior)." Mid-America Transportation Center.

ACI-318 (2014). "Building Code Requirements for Structural Concrete (ACI 318-14) and Commentary on Building Code Requirements for Structural Concrete (ACI 318R-14)."

ACI (2017). "Guide for the Design and Construction of Externally Bonded FRP Systems for Strengthening Concrete Structures (ACI 440-2R-17)." American Concrete Institute Farmington Hills, MI, USA.

Ahmed, A., and Masmoudi, R. (2018). "Axial Response of Concrete-Filled FRP Tube (CFFT) Columns with Internal Bars." *Journal of Composites Science*, 2(4), 57.

Aslani, F., Gunawardena, Y., and Dehghani, A. (2019). "Behaviour of concrete filled glass fibre-reinforced polymer tubes under static and flexural fatigue loading." *Construction and Building Materials*, 212, 57-76.

ASTM-C192/C192M-16 (2016). "Standard Practice for Making and Curing Concrete Test Specimens in the Laboratory." ASTM International, West Conshohocken, PA.

ASTM-C1437 (2007). "Standard test method for flow of hydraulic cement mortar." *C 1437*.

ASTM-International-E8/E8M-13 (2013). "Standard Test Methods for Tension Testing of Metallic Materials." West Conshohocken, PA, ASTM International.

Bae, B.-I., Choi, H. K., and Choi, C. S. (2016). "Bond stress between conventional reinforcement and steel fibre reinforced reactive powder concrete." *Construction and Building Materials*, 112, 825-835.

Bakis, C. E., Bank, L. C., Brown, V., Cosenza, E., Davalos, J., Lesko, J., Machida, A., Rizkalla, S., and Triantafillou, T. (2002). "Fiber-reinforced polymer composites for construction—State-of-the-art review." *Journal of composites for construction*, 6(2), 73-87.

Bandelt, M. J., Frank, T. E., Lepech, M. D., and Billington, S. L. (2017). "Bond behavior and interface modeling of reinforced high-performance fiber-reinforced cementitious composites." *Cement and Concrete Composites*, 83, 188-201.

Beaulieu, L.-V., Legeron, F., and Langlois, S. (2010). "Compression strength of corroded steel angle members." *Journal of Constructional Steel Research*, 66(11), 1366-1373.

Belzer, B., Robinson, M., and Fick, D. (2013). "Composite action of concrete-filled rectangular GFRP tubes." *Journal of Composites for Construction*, 17(5), 722-731.

Bruneau, M., Uang, C.-M., and Whittaker, A. (1998). *Ductile design of steel structures*, McGraw-Hill New York.

Bruneau, M., and Zahrai, S. M. (1997). "Effect of severe corrosion on cyclic ductility of steel." *Journal of Structural Engineering*, 123(11), 1478-1486.

de Larrard, F., and Sedran, T. (1994). "Optimization of ultra-high-performance concrete by the use of a packing model." 24(6), 997-1009.

Donchev, T., Srebrenkoska, V., Petkova, D., Albkeirat, M., and Akhundzada, H. "Behaviour of column constructed with FRP tubes filled with concrete." *Proc., MATEC Web of Conferences*, EDP Sciences, 04001.

du Béton, F. I. (2000). "Bond of reinforcement in concrete: state-of-art report." *Bulletin* 10, 160-167.

ElGawady, M., Booker, A. J., and Dawood, H. M. (2010). "Seismic behavior of posttensioned concrete-filled fiber tubes." *Journal of Composites for Construction*, 14(5), 616-628.

Fam, A., Cole, B., and Mandal, S. (2007). "Composite tubes as an alternative to steel spirals for concrete members in bending and shear." *Construction and Building Materials*, 21(2), 347-355.

Fam, A., Flisak, B., and Rizkalla, S. (2003). "Experimental and analytical modeling of concrete-filled FRP tubes subjected to combined bending and axial loads." *ACI Struct. J*, 100(4), 499-509.

Fam, A., and Rizkalla, S. H. (2001). "Behavior of axially loaded concrete-filled circular FRP tubes." *Aci Struct J*, 98(3), 280-289.

Fam, A., Schnerch, D., and Rizkalla, S. (2005). "Rectangular filament-wound glass fiber reinforced polymer tubes filled with concrete under flexural and axial loading: experimental investigation." *Journal of Composites for Construction*, 9(1), 25-33.

Fam, A. Z., and Rizkalla, S. H. (2001). "Confinement model for axially loaded concrete confined by circular fiber-reinforced polymer tubes." *Structural Journal*, 98(4), 451-461.

Fam, A. Z., and Rizkalla, S. H. (2002). "Flexural behavior of concrete-filled fiber-reinforced polymer circular tubes." *Journal of Composites for Construction*, 6(2), 123-132.

Farhat, F., Nicolaides, D., Kanellopoulos, A., and Karihaloo, B. L. (2007). "High performance fibre-reinforced cementitious composite (CARDIFRC)–Performance and application to retrofitting." *Engineering Fracture Mechanics*, 74(1-2), 151-167.

Farzad, M., Shafieifar, M., and Azizinamini, A. (2018). "Accelerated Retrofitting of Bridge Elements Subjected to Predominantly Axial Load Using UHPC Shell."

FHWA (2015). "National Bridge Inventory." *U.S. Department of Transportation, Federal Highway Administration*.

Graybeal, B. (2011). "Ultra-high performance concrete." *No. FHWA-HRT-11-038. 2011*.

Hadi, M. N. (2008). "Bond of high strength concrete with high strength reinforcing steel."

Hannigan, P. J., Rausche, F., Likins, G., Robinson, B., Becker, M., and Berg, R. R. (2016). "Design and construction of driven pile foundations–Volume I." National Highway Institute (US).

Harajli, M. (2009). "Bond stress–slip model for steel bars in unconfined or steel, FRC, or FRP confined concrete under cyclic loading." *Journal of structural engineering*, 135(5), 509-518.

Hu, A., Liang, X., and Shi, Q. (2020). "Bond Characteristics between High-Strength Bars and Ultrahigh-Performance Concrete." *Journal of Materials in Civil Engineering*, 32(1), 04019323.

Ichikawa, S., Matsuzaki, H., Moustafa, A., ElGawady, M. A., and Kawashima, K. (2016). "Seismic-resistant bridge columns with ultrahigh-performance concrete segments." *Journal of Bridge Engineering*, 21(9), 04016049.

Jiang, X., and Soares, C. G. (2012). "A closed form formula to predict the ultimate capacity of pitted mild steel plate under biaxial compression." *Thin-Walled Structures*, 59, 27-34.

Jiang, X., and Soares, C. G. (2012). "Ultimate capacity of rectangular plates with partial depth pits under uniaxial loads." *Marine Structures*, 26(1), 27-41.

Karagah, H., Shi, C., Dawood, M., and Belarbi, A. (2015). "Experimental investigation of short steel columns with localized corrosion." *Thin-Walled Structures*, 87, 191-199.

Kayser, J. R., and Nowak, A. S. (1989). "Capacity loss due to corrosion in steel-girder bridges." *Journal of Structural Engineering*, 115(6), 1525-1537.

Liu, X., Nanni, A., and Silva, P. F. (2005). "Rehabilitation of compression steel members using FRP pipes filled with non-expansive and expansive light-weight concrete." *Advances in Structural Engineering*, 8(2), 129-142.

Mirmiran, A., and Shahawy, M. (1997). "Behavior of concrete columns confined by fiber composites." *Journal of Structural Engineering*, 123(5), 583-590.

Mohamed, H. M., and Masmoudi, R. (2010). "Flexural strength and behavior of steel and FRP-reinforced concrete-filled FRP tube beams." *Engineering Structures*, 32(11), 3789-3800.

Ok, D., Pu, Y., and Incecik, A. (2007). "Computation of ultimate strength of locally corroded unstiffened plates under uniaxial compression." *Marine Structures*, 20(1), 100-114.

Paik, J., Lee, J., and Ko, M. (2003). "Ultimate compressive strength of plate elements with pit corrosion wastage." *Proceedings of the Institution of Mechanical Engineers, Part M: Journal of Engineering for the Maritime Environment*, 217(4), 185-200.

Perry, V. (2006). "Ductal®-A Revolutionary New Material for New Solutions. Association of Professional Engineers and Geoscientists of the Province of Manitoba (APEGM)."

Ramadan, A. (2020). "Assessment and retrofitting of corroded steel H-piles " Ph.D., Missouri University of Science and Technology.

Ramadan, A., and ElGawady, M. "Axial behavior of corroded H-Piles." *Proc., Proc., IABSE Congress*.

Raynor, D. J., Lehman, D. E., and Stanton, J. F. (2002). "Bond-slip response of reinforcing bars grouted in ducts." *Structural Journal*, 99(5), 568-576.

Romanoff, M. (1962). *Corrosion of steel pilings in soils*, US Government Printing Office.

Saad-Eldeen, S., Garbatov, Y., and Soares, C. G. (2011). "Experimental assessment of the ultimate strength of a box girder subjected to severe corrosion." *Marine Structures*, 24(4), 338-357.

Shafieifar, M., Farzad, M., and Azizinamini, A. (2017). "Experimental and numerical study on mechanical properties of Ultra High Performance Concrete (UHPC)." *Construction and Building Materials Volume 156,402-411*.

Shrestha, B., Gheni, A., Abdulazeez, M. M., and ElGawady, M. A. (2020). "Innovative Approach to Repair Corroded Steel Piles using Ultra-High Performance Concrete." *Transportation Research Record*, 0361198120929329.

Stauffer, S. T. (2016). "Performance Assessment of Deteriorated and Retrofitted Steel HP Piles."

Wan, B. (2013). "Procedures, Cost and Effectiveness for Deteriorated Bridge Substructure Repair." Wisconsin Highway Research Program.

Wille, K., Naaman, A. E., and Parra-Montesinos, G. J. J. A. m. j. (2011). "Ultra-High Performance Concrete with Compressive Strength Exceeding 150 MPa (22 ksi): A Simpler Way." 108(1).

Wipf, T. J., Fanous, F., Klaiber, F., and Eapen, A. (2003). "Evaluation of Appropriate Maintenance, Repair and Rehabilitation Methods for Iowa Bridges." *Final Report, Iowa DOT Project TR-429*.